JACS
JOURNAL OF THE AMERICAN CHEMICAL SOCIETY
pubs.acs.org/JACS
Article

A Local Structure Analysis of Defects in UiO-66: Insights from Solid-State Nuclear Magnetic Resonance and X-ray Absorption Fine Structure

Jiabin Xu, Kun Feng, Wanli Zhang, Amrit Venkatesh, Ivan Hung, Yuzhen Liu, Jingyan Liu, Shuting Li, Giuliana Battiston, Zhehong Gan, Shoushun Chen, Yun-Mui Yiu, Jun Zhong,* Tsun-Kong Sham,* and Yining Huang*

Cite This: J. Am. Chem. Soc. 2025, 147, 44200−44215

Read Online

ACCESS | Metrics & More | Article Recommendations | Supporting Information

ABSTRACT: Defect engineering in metal−organic frameworks (MOFs) offers a promising approach to modify material properties by introducing controlled structural imperfections. Zr-based MOFs, particularly the well-known UiO-66, hold significant potential for diverse applications. Defects in UiO-66 can be generated using monocarboxylic acids as modulators, among other methods. However, resolving the atomic-level local structures of these defects remains a considerable challenge. In this study, the local structures of these defects are carefully characterized by multinuclear solid-state NMR spectroscopy (SSNMR) in combination with X-ray absorption fine structure (XAFS). In situ heating XAFS analyses at Zr K-edge reveal critical changes in the local structure of Zr during the removal of trifluoroacetic acid (TFA), including the decreased Zr−O coordination numbers and alterations in Zr−Zr bond distances. Multinuclear ^{1}H, ^{13}C, ^{19}F, $^{35/37}Cl$, ^{17}O solid-state NMR methods are used to identify capping species and defect-associated species. Subsequently, the engineered defects are found to significantly improve the catalytic performance of Pt nanoparticles (NPs) integrated into the defective UiO-66 framework. Pt-UiO-66 with defects exhibits much improved hydrogen evolution reaction (HER) activity and stability compared to the Pt-UiO-66 without defects.

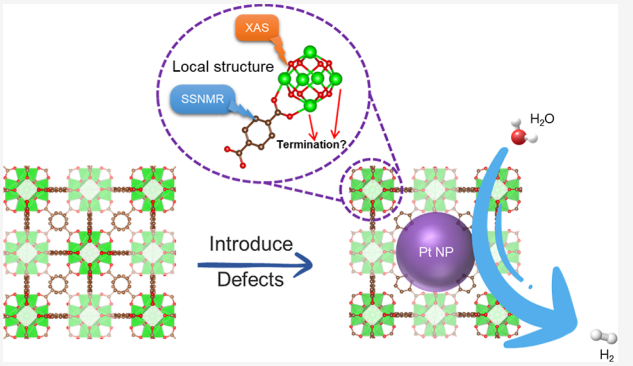

INTRODUCTION

While perfection is often revered as the ultimate pursuit in material design, it is the presence of imperfections that sometimes unlocks unexpected potential and new functionalities. Structural imperfections or defects, far from being mere flaws, can pose beneficial effects on physical and chemical properties of materials. In semiconductors, for instance, defects are deliberately introduced to tailor their electronic structures for optoelectronic and catalytic applications.[1,2] This concept, known as defect engineering, has emerged as a versatile strategy for material modification through judicious control over defect formation. Metal−organic frameworks (MOFs), known for their structural tunability and chemical versatility, provide an ideal platform for defect engineering. Among them, UiO-66 ($Zr_6O_4(OH)_4(BDC)_6$, BDC = benzene-1,4-dicarboxylate), a Zr-based MOF built from robust Zr_6 cornerstones, stands out due to its high connectivity and remarkable thermal and chemical stability.[3−6] Starting in 2011,[7] UiO-66 has attracted extensive attention for its ability to accommodate a high concentration of structural defects without compromising its original crystal structure.[8] This is primarily achieved through the partial substitution of BDC linkers with monocarboxylic modulators such as formic acid (FA), acetic acid (AA), difluoroacetic acid (DFA), trifluoroacetic acid (TFA) and benzoic acid (BA).[9] The introduction of such defects generates coordinatively unsaturated metal sites serving as Lewis acid sites, which is beneficial for adsorptive or catalysis performance.[10−14]

In this context, it is necessary to point out that the defects in UiO-66 can be typically classified into two types: missing linker and missing cluster defects.[15−18] The ideal, defect-free UiO-66 features a 12-connected $[Zr_6O_4(OH)_4]^{12+}$ cluster, where each BDC linker bridges two neighboring clusters, forming the *fcu* topology (Scheme 1). Within each cluster, four μ_3−OH^- and four μ_3−O^{2-} groups bridge the Zr^{4+} ions. Missing linker

Received: August 10, 2025
Revised: November 9, 2025
Accepted: November 12, 2025
Published: November 18, 2025

https://doi.org/10.1021/jacs.5c13805
J. Am. Chem. Soc. 2025, 147, 44200−44215

Scheme 1. Structure of Defect-Free UiO-66[a]

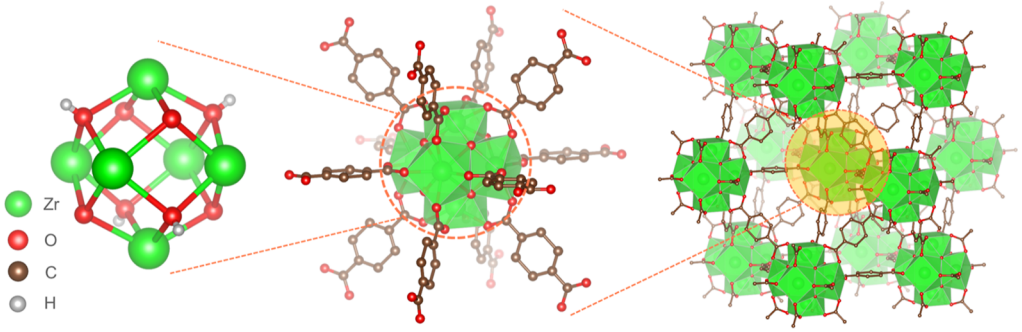

[a]The $[Zr_6O_4(OH)_4]^{12+}$ cluster is coordinated by 12 BDC linkers, forming a highly connected framework in which each cluster is further surrounded by 12 neighboring clusters.

defects arise from partial substitution of dicarboxylate linkers by monocarboxylate modulators, while missing cluster defects occur when an entire $[Zr_6O_4(OH)_4]^{12+}$ node is absent. The latter creates large mesoporous cages (~1.8 nm in diameter) and gives rise to a different topology, known as the *reo* topology.[15,18]

Despite the growing interest in defective UiO-66 for diverse applications, the fundamental structure and nature of these defects remain not fully understood. A main debate lies in which species compensate for the defect sites and how charge balance is achieved.[19−21] Proposed defect-compensating species include monocarboxylic modulators, OH^-,[22] Cl^-,[23,24] H_2O,[19,22] DMF,[7] or combinations thereof.[25] For example, Shearer et al. identified deprotonated modulators and formate (from DMF decomposition) as likely compensating species based on solution ^1H NMR spectra.[9] In contrast, Zhao et al. suggested that Cl^- may coordinate with defective Zr sites, as evidenced by energy-dispersive X-ray spectroscopy (EDS) mapping.[24] However, these conflicting interpretations are largely due to variations in synthesis conditions and postsynthetic treatments. In fact, postsynthetic treatments such as activation and solvent exchange can significantly alter the defect environment. For instance, Tan et al. reported that both H_2O and acetic acid modulator bond to two adjacent Zr^{4+} vacancies, which undergoes a unidentate-to-bidentate transition after water is removed by heating.[19] On the other hand, high-temperature activation can lead to the removal of modulators, e.g., TFA is eliminated at 320 °C.[26−28] This process is accompanied by dehydroxylation of $[Zr_6O_4(OH)_4]^{12+}$ clusters. All things considered, the complexities underscore the need for a more comprehensive investigation into the defect structures of UiO-66 at the molecular level.

It should be pointed out that no single technique can fully capture the structural and chemical complexity of defective UiO-66, as each provides a unique yet inherently partial perspective. Solid-state nuclear magnetic resonance spectroscopy (SSNMR) has been widely employed in the study of UiO-66 for elucidating structural details and probing host−guest interactions. For example, both 1D and 2D ^1H and ^{13}C SSNMR experiments have been used to analyze the local environments of functionalized UiO-66 framework bearing −Br, $-CH_3$, −OH, and $-NH_2$ groups.[29,30] ^1H and ^{13}C SSNMR have also been applied to investigate the interactions between guest molecules (alkanes, DMF, H_2O, acetone, methanol, and cyclohexane) and the framework, including the identification of binding or adsorption sites.[31−33] ^{19}F and ^{17}O SSNMR offer insights into the local environments of fluorinated[26−28] and oxygen-containing species.[34,35] In addition, ^2H SSNMR has been employed to investigate linker dynamics in UiO-66 in the presence of benzene as a guest molecule.[36] Despite these valuable applications, SSNMR has not been systematically used for defect characterization in UiO-66, primarily due to the complexity of various species associated with defects. One notable example is ^{91}Zr SSNMR, which can provide insight into local structural disorder and the influence of guest species on Zr centers.[37,38] However, its application in defect characterization is limited by challenges in data acquisition and interpretation, due to the low natural abundance, low gyromagnetic ratio, and relatively large quadrupole moment of ^{91}Zr nuclei.[39] Furthermore, the porous nature of MOFs results in a significant weight dilution of Zr centers, further weakening signal detection. Consequently, our previous attempts to investigate missing-linker defects in UiO-66 using ^{91}Zr solid-state NMR proved challenging.[38]

In contrast, X-ray absorption fine structure (XAFS) offers a complementary perspective on defect structures by directly probing the local coordination environment of Zr centers, including bond distances, coordination numbers, and structural disorder. This makes it particularly suitable for tracking cluster dehydroxylation or distortion during thermal activation. Previous XAFS studies on UiO-66 have revealed that dehydroxylation distorts the local structure of $[Zr_6O_4(OH)_4]^{12+}$ clusters, transforming them into $[Zr_6O_6]^{12+}$ clusters with shorter Zr−O bonds and a reduced coordination number from eight to seven.[7] However, XAFS also has its limitations. While it can detect changes such as Zr−O bond shortening or coordination number reduction, it cannot easily distinguish whether the compensating species is a modulator, hydroxyl, chloride, or water because such species are present in low concentrations relative to linkers, and thus their signals are likely averaged out among the dominant surrounding oxygen atoms from linkers. In addition, XAFS is insensitive to light elements like hydrogen, limiting its ability to probe hydroxyl-related chemistry directly. A more detailed comparison and complementarity of these two approaches is summarized in Table S1.

X-ray diffraction (XRD) provides long-range structural information and is widely used to evaluate the crystallinity and phase purity of UiO-66. Both synchrotron-based powder XRD and single-crystal XRD has been used to study the hydroxylated and dehydroxylated forms of UiO-66, as well as

https://doi.org/10.1021/jacs.5c13805
J. Am. Chem. Soc. 2025, 147, 44200−44215

frameworks containing missing linker defects.[7,22] Missing cluster defects can also be identified by the appearance of two weak diffraction peaks at around 4° and 6°, which are characteristic of the *reo* phase.[15,18,40] Nevertheless, conventional XRD cannot directly resolve the detailed local structure of defects or subtle distortions, particularly those introduced upon postsynthetic modification. Despite this limitation, XRD provides essential information on the overall framework architecture and, when combined with SSNMR and XAFS, offers structural context that links local chemical environments with the global lattice structure.

Other techniques, including TGA and BET, provide additional insights into composition, porosity, and surface area but capture only fragments of the overall picture. The true strength of defect characterization lies in the integration of multiple methods.

Herein, we present a comprehensive investigation of the defect-associated species and local structure in UiO-66, using a combination of multiple techniques. By integrating a suite of complementary techniques, including SSNMR, XAFS, XRD, N_2 adsorption, FT-IR, HAADF-STEM, and DFT modeling, we achieved molecular-level chemical specificity alongside atomic-level structural insights. The convergence of evidence from these diverse methodologies provides a coherent and well-corroborated picture of how defects form, evolve, and function in UiO-66.

Following established procedures,[26−28] we synthesized a highly defective UiO-66 featuring both missing linker and missing cluster defects by using TFA as a modulator. A series of samples, including pristine (UiO-66-TFA-asmade), desolvated (UiO-66-TFA-act200), and dehydroxylated (UiO-66-TFA-act320) states, were systematically characterized by SSNMR experiments, including $^{1}H-^{13}C$ cross-polarization (CP) magic angle spinning (MAS), $^{19}F-^{13}C$ CP MAS NMR, ^{1}H, ^{17}O, and ^{19}F MAS NMR, and the 2D $^{1}H-^{1}H$ double quantum to single quantum (DQ−SQ), single quantum to single quantum (SQ−SQ), ^{17}O triple quantum MAS (3QMAS) NMR. It is found that TFA and water molecules are initially coordinated to the adjacent defective Zr^{4+} sites in the pristine form (UiO-66-TFA-asmade). Upon activation at 200 °C (UiO-66-TFA-act200), TFA molecules transform from monodentate to bidentate coordination. Complete TFA removal at 320 °C (UiO-66-TFA-act320) along with dehydroxylation results in the formation of coordinately unsaturated Zr^{4+} sites. These sites are likely charge-compensated by Cl^{-} ions originating from the hydrolysis of the $ZrCl_4$ precursor. Postsynthetic modification, such as ion exchange or water readsorption, enables reintroduction of terminal species like μ_1-OH^{-}, and reverses $[Zr_6O_6]^{12+}$ clusters back to $[Zr_6O_4(OH)_4]^{12+}$, demonstrating the reversible nature of these defect structures.

In situ XAFS measurements provided further atomic-level insight into the local coordination environment, showing that defective UiO-66 possesses a more distorted $[Zr_6O_6]^{12+}$ cluster geometry with shorter average Zr−O and Zr−Zr distances, and a reduced Zr−O coordination number compared to the defect-free UiO-66.

As a practical demonstration of the significance of these defects created in our study, we explored their role in hosting small Pt NPs for the hydrogen evolution reaction (HER), which converts water into hydrogen. The defect-rich UiO-66 facilitates uniform dispersion of Pt NPs by providing anchoring sites and suppresses their aggregation through a confinement effect, as evidenced by high-angle annular dark-field scanning transmission electron microscopy (HAADF-STEM) and elemental mapping. Consequently, Pt-loaded defective UiO-66 exhibits enhanced HER catalytic activity and long-term stability compared to its defect-free counterpart. These findings highlight the crucial role of defects in modulating the local structure and functionality of MOFs and point to their broader potential in future applications.

RESULTS

Pristine UiO-66 samples, both defective and defect-free, were synthesized via a solvothermal method with minor modifications based on literature procedures.[9] The details are given in the Experimental section. The defect-free sample is denoted as UiO-66-asmade, while the defective sample, prepared using TFA as a modulator, is referred to as UiO-66-TFA-asmade. Activation at 200 and 320 °C is commonly employed to remove residual solvent molecules (such as DMF and water) from the MOF pores and to eliminate coordinated TFA (which also induces dehydroxylation), respectively.[26−28] Our ^{1}H MAS NMR spectra (Figure S1) directly verify that the literature-reported temperatures are appropriate for our samples. Accordingly, the resulting desolvated and dehydroxylated samples are labeled UiO-66-TFA-act200 and UiO-66-TFA-act320 for defective MOFs, and UiO-66-act200 and UiO-66-act320 for defect-free counterparts. A summary of sample designations and corresponding treatment conditions is provided in Table S2. Defect formation in UiO-66 arises from the competitive coordination between modulator molecules and BDC linkers at Zr sites. The effectivity relies on the type and amount of modulator used.[8] In this study, TFA was chosen due to its low pK_a value of 0.23, which enable stronger competition for coordination sites through enhanced deprotonation compared to BDC linkers (pK_{a1} = 3.51, pK_{a2} = 4.82) and other commonly used monocarboxylic acids, such as FA (pK_a = 3.77), AA (pK_a = 4.76), DFA (pK_a = 1.24), BA (pK_a = 4.21).[9] To maximize defect incorporation, 30 equiv of TFA relative to BDC linker were added during synthesis. The theoretical maximum number of missing linkers induced by monocarboxylic acid is ∼4.3 per cluster, where the total number of linkers per cluster is 12.[41,42]

Thermogravimetric analysis (TGA) has been recognized as one of the most effective ways to estimate defect concentrations by comparing the mass loss associated with the decomposition of UiO-66 to the theoretical molecular weight of its fully dehydroxylated form, $Zr_6O_6(BDC)_6$, which is 2.2 times heavier than the final $6ZrO_2$ product.[23,28,43] The difference between this theoretical value and the experimentally determined weight loss indicates the degree of defect creation. Based on TGA results in Figure S2, the defect concentration of UiO-66-TFA is calculated to be ∼27%, corresponding to an average of 4 missing linkers per Zr_6O_6 cluster. Despite the high degree of missing linkers, XRD results (Figure S3a) suggest the UiO-66-TFA framework retains its crystallinity and matches well with the simulated data, even after dehydroxylation. Moreover, synchrotron-based XRD reveals the presence of missing cluster defects in UiO-66-TFA, evidenced by two weak and broad Bragg diffraction peaks at low angles around 4° and 6°, which are characteristic of the *reo* topology (Figure S3b).[15,18] Additionally, nitrogen adsorption measurements (Figure S4a,b) reveal that UiO-66-TFA-act200 and UiO-66-TFA-act320 have reduced surface areas compared to their defect-free counterparts. The pore size

https://doi.org/10.1021/jacs.5c13805
J. Am. Chem. Soc. 2025, 147, 44200−44215

Scheme 2. Schematic Diagram of UiO-66 with TFA as a Modulator, Highlighting the Transition Process During Thermal Activation[a]

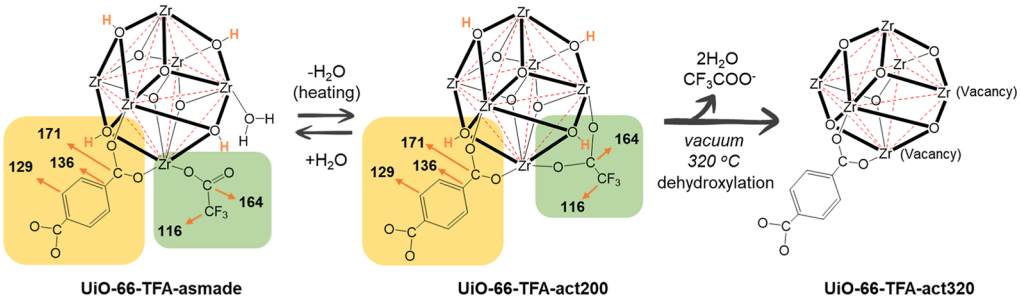

[a]The diagram focuses on the local structure of a pair of defect sites (i.e., two unsaturated Zr^{4+} centers) terminated by TFA molecules. The yellow-shaded region shows the main detectable area by $^{1}H-^{13}C$ CP MAS, while the green-shaded part shows the main detectable area by $^{19}F-^{13}C$ CP MAS. Upon activation at 320 °C, TFA is removed, and the vacancies are created.

distribution (Figure S4c,d) also shows additional features around 2 nm in the defective UiO-66 samples, which is consistent with missing-cluster defects that generate larger pores than those in the defect-free structure.[18]

Local Structure of Pristine UiO-66-TFA-Asmade. As mentioned above, the precise identity of defect-terminating species remains unclear. In addition to modulator molecules, H_2O, OH^- and/or Cl^- ions may also be involved in charge compensation at defect sites. To this end, SSNMR is used to directly detect local environments of potential defect-related species. The possible termination configurations in UiO-66-TFA-asmade are illustrated in Figure S5. Assuming that TFA coordinates to Zr (Scheme 2), we acquired $^{1}H-^{13}C$ CP MAS and direct excitation ^{13}C MAS spectra with ^{1}H and ^{19}F decoupling, respectively, for UiO-66-TFA-asmade (Figures 1a and S6a,b). Resonances at 171, 136, and 129 ppm are assigned to the carboxyl carbons, quaternary aromatic carbons and the aromatic C−H carbons of the BDC linkers, respectively (Scheme 2, yellow region).[30,44,45] Peaks at 163, 37, and 31 ppm indicate the presence of residual DMF within the MOF pores.[33,46] Compared to a solid CF_3COONa reference (Figure S6c), the peaks at 164 and 116 ppm can be assigned to the carboxylic and CF_3 groups of TFA, respectively.[47] Note that the resonances of the carbonyl carbon of DMF and carboxylic carbon of TFA overlap at ca. 164 ppm. Note also that the 116 ppm peak corresponding to CF_3 group in ^{13}C MAS spectrum does not appear in the $^{1}H-^{13}C$ CP MAS NMR spectrum (Figure 1a).

Fluorine atoms from TFA can be directly detected via ^{19}F MAS NMR (Figure 1c). In the spectrum of UiO-66-TFA-asmade, the dominant peaks can be deconvoluted into two peaks at −75.5 and −77.0 ppm, which are attributed to physically adsorbed TFA molecules and dangling TFA coordinated to a single Zr^{4+} site, respectively (Scheme 2, green area in UiO-66-TFA-asmade), consistent with previous studies reporting two peaks at −75 and −78 ppm.[26−28] ^{1}H SSNMR spectroscopy provides additional structural information on H_2O and OH^-. As shown in Figures 2b and S7, both UiO-66-TFA-asmade and UiO-66-asmade exhibit similar spectra, with a broad peak at ca. 4.5 ppm attributed to residual water. A peak at ca. 8.0 ppm corresponds to aromatic protons of the BDC ligands, while two sharp peaks at ca. 2.2 and 1.9 ppm belong to residual DMF.[30,33,48] A small peak at 7.1 ppm can also be assigned to DMF or free BDC ligands.[33]

To further explore whether oxygen-containing species are present at defect sites and whether their local environments are

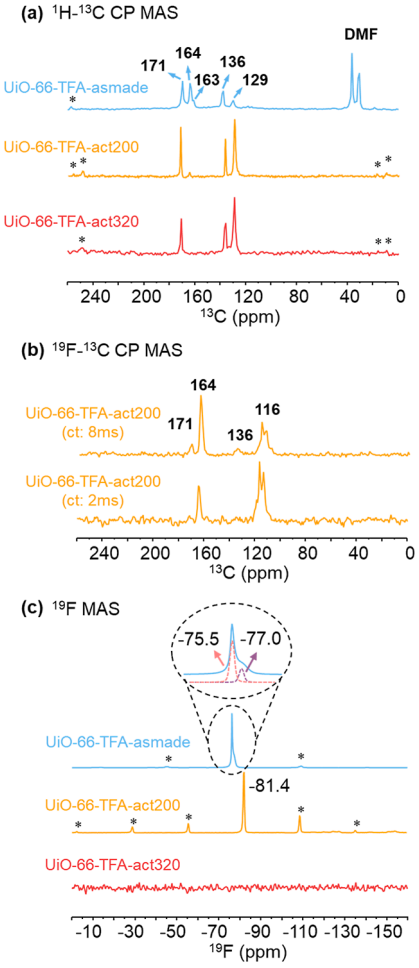

Figure 1. (a) $^{1}H-^{13}C$ CP MAS NMR spectra of UiO-66-TFA at different process stages obtained at a spinning rate of 12 kHz and a contact time of 8 ms: UiO-66-TFA-asmade, UiO-66-TFA-act200, UiO-66-TFA-act320. (b) $^{19}F-^{13}C$ CP MAS NMR spectra of UiO-66-TFA-act200 obtained at a spinning rate of 10 kHz and contact times of 2 and 8 ms. Note that signal of the CF_3 groups appears as multiplets at 116 ppm since the spectra are acquired without fluorine decoupling. (c) ^{19}F MAS NMR spectra of UiO-66-TFA-asmade, UiO-66-TFA-act200 and UiO-66-TFA-act320. The inset shows an enlarged view, revealing that the peak consists of two overlapping individual peaks. Note that the asterisk (*) represents the spinning sidebands.

https://doi.org/10.1021/jacs.5c13805
J. Am. Chem. Soc. 2025, 147, 44200−44215

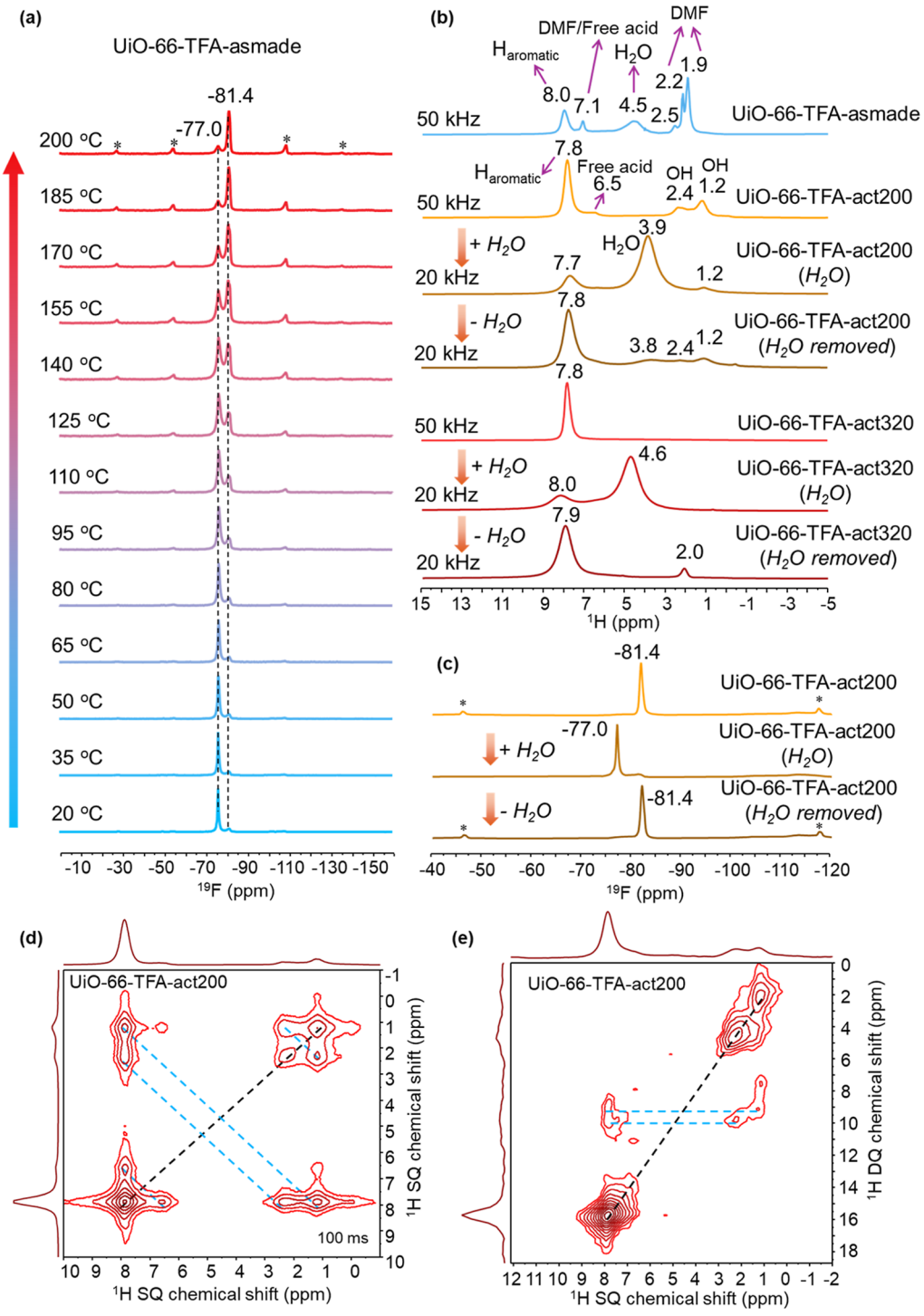

Figure 2. (a) In situ ^{19}F MAS NMR spectra of UiO-66-TFA-asmade as a function of temperature from room temperature to high temperature (200 °C). Asterisk (*) represents the spinning sidebands. (b) ^{1}H MAS NMR spectra of UiO-66-TFA under different conditions obtained at spinning rates of 20 and 50 kHz. (c) Corresponding ^{19}F MAS NMR spectra of UiO-66-TFA-act200 under different conditions at a spinning rate of 20 kHz. (d) 2D ^{1}H−^{1}H SQ−SQ spectra of UiO-66-TFA-act200 acquired with mixing time of 100 ms. (e) 2D ^{1}H−^{1}H DQ−SQ BABA spectra of UiO-66-TFA-act200 with one rotor period (20 μs) for excitation and reconversion blocks.

affected by defects, we also carried out ^{17}O SSNMR experiments as ^{17}O NMR is an effective probe for the local environment of oxygen-containing groups in UiO-66.[34,35] However, ^{17}O is a spin-5/2 quadrupolar nucleus with a very low natural abundance (0.037%), which makes data acquisition at natural abundance highly challenging. Therefore, ^{17}O-enriched samples were prepared by adding $H_2{}^{17}O$ (40 atom % enriched) as the ^{17}O source during synthesis, allowing isotopic exchange with oxygen species in the framework (see Supporting Information for the degree of ^{17}O enrichment). As shown in the ^{17}O spectrum of UiO-66-TFA-asmade (Figure 3a), three distinct signals are observed and assigned to carboxylate oxygens, μ_3−O^{2-} and μ_3−OH^{-} groups, respectively.[34,35] An additional small peak in UiO-66-asmade is

https://doi.org/10.1021/jacs.5c13805
J. Am. Chem. Soc. 2025, 147, 44200−44215

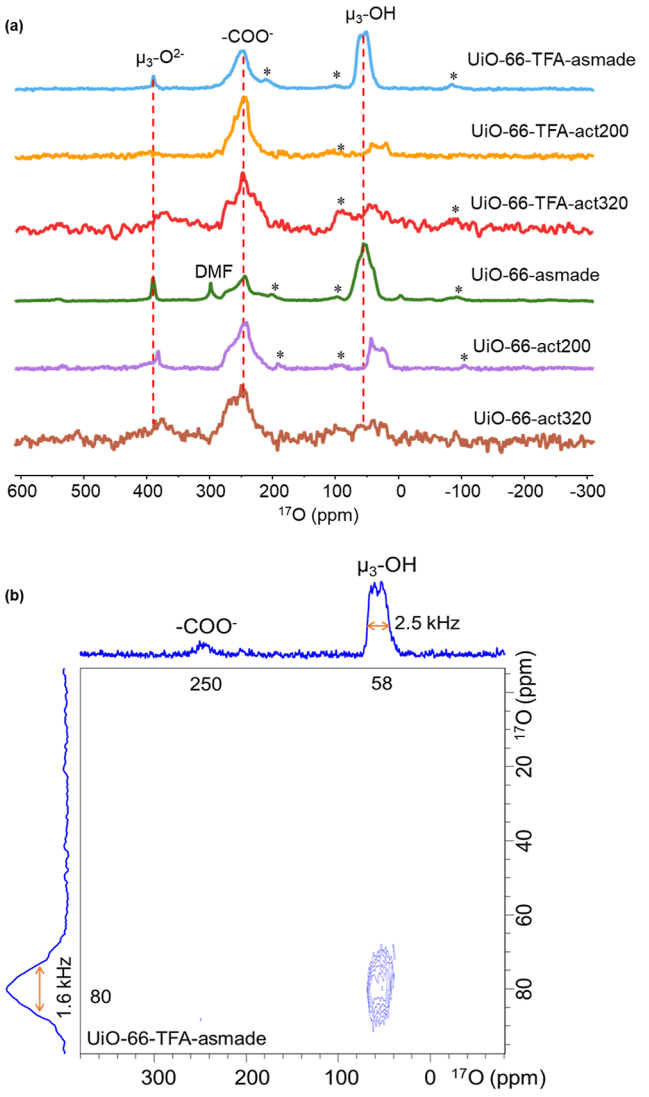

Figure 3. (a) ^{17}O MAS NMR spectra of a series of UiO-66-TFA and UiO-66 at a magnetic field of 18.8 T acquired at a spinning frequency of 16 kHz. Note that asterisk (*) represents the spinning sidebands. (b) 2D ^{17}O 3QMAS NMR spectrum of UiO-66-TFA-asmade.

attributed to residual DMF in the pores. Furthermore, the 2D ^{17}O 3QMAS spectrum of UiO-66-TFA-asmade (Figure 3b) exhibits a broad symmetric isotropic peak associated with μ_3−OH^- in the indirect F1 dimension. The extracted slices at different F1 positions indicate a small, but noticeable distribution of chemical shift (see Figure S8 and its caption for details). The broadness of this peak reflects a distribution of slightly different environments in $[Zr_6O_4(OH)_4]^{12+}$ clusters, likely caused by the distribution of TFA ions at nearby defect sites.

Overall, the TFA modulator introduced replaces several BDC linkers during synthesis, as illustrated in Scheme 3 (from a to b). In UiO-66-TFA-asmade, in addition to residual DMF and TFA molecules physically adsorbed inside the pores, a TFA molecule is coordinated to one Zr^{4+} site in a monodentate fashion, while a water molecule coordinates to an adjacent Zr^{4+} site. The presence of these compensating species results in slightly different local environments for μ_3−OH^- groups in the $[Zr_6O_4(OH)_4]^{12+}$ clusters, as evidenced by ^1H and ^{17}O 3QMAS spectra, in contrast to the single, symmetric μ_3−OH^- environment observed in defect-free UiO-66-asmade.

Local Structure of Desolvated UiO-66-TFA-act200. To rule out the effect of remaining solvents (such as DMF and H_2O) inside the pores, the samples are activated at 200 °C. As shown in ^1H−^{13}C CP MAS NMR spectra of UiO-66-TFA-act200 (Figure 1a), all residual DMF molecules are removed since the resonances due to methyl groups of DMF disappeared. However, the signal at ∼164 ppm persists. This resonance, therefore, can only be attributed to TFA (green area in Scheme 2). Apparently, it overlaps with the peak due to DMF before activation. ^{19}F−^{13}C CP MAS spectra (Figure 1b) were also acquired with two contact times. At a short contact time of 2 ms, only the characteristic peaks of TFA are detected after solvent removal. At a longer contact time of 8 ms, additional signals from neighboring BDC ligands (171 and 136 ppm) appear, indicating that TFA is not too far from the BDC linkers. These results complement the observations in the corresponding ^1H−^{13}C CP MAS spectrum, confirming that TFA is attached to the MOF framework. In the ^{19}F MAS spectrum of UiO-66-TFA-act200, only one peak at −81.4 ppm appears with multiple spinning sidebands. This signal is assigned to TFA molecules that have converted from unidentate to bidentate coordination, bridging two neighboring Zr^{4+} sites (Scheme 2, green area). To further support this assignment, we performed DFT calculations of the ^{19}F NMR chemical shifts, and the predicted trend is consistent with our experimental results (Figure S9). Compared to UiO-66-TFA-asmade, which exhibits weaker and fewer spinning sidebands due to higher mobility, the significant number of sidebands observed in the spectrum of UiO-66-TFA-act200 reflect increased chemical shift anisotropy (CSA) due to reduced mobility of the TFA molecules, consistent with restricted rotational freedom in the bidentate mode. To further verify this unidentate ⇋ bidentate transformation, in situ variable temperature (VT) ^{19}F MAS experiments were conducted. As shown in Figure 2a, a dominant peak at −77.0 ppm is observed along with a minor peak at −81.4 ppm at room temperature. Upon heating, the removal of water from the adjacent Zr^{4+} site (confirmed by ^1H spectra below in Figure 2b) drives the equilibrium toward the bidentate form. Consequently, the peak at −81.4 ppm intensifies while the peak at −77.0 ppm vanishes with increasing temperature. In addition, we find this process is reversible. After exposing UiO-66-TFA-act200 to atmospheric moisture overnight, a signal at −77.0 ppm appears (Figure S10), supporting the reformation of unidentate TFA. This observation highlights the strong water affinity of defective UiO-66 and the reversibility of the unidentate/bidentate transformation, driven by water adsorption and desorption at the Zr site.

In ^1H MAS spectra (Figure 2b), aromatic ^1H signals at 7.8 ppm dominate, and bridging μ_3−OH^- group signals emerge in the range of 0−3 ppm.[30,33,37] In contrast to defect-free UiO-66-act200, where there is only one μ_3−OH^- signal at 2.0 ppm (Figure S7), there are two μ_3−OH^- signals (2.4 and 1.2 ppm) due to coordinated TFA breaking the entire symmetry of $[Zr_6O_4(OH)_4]^{12+}$ clusters. One of the μ_3−OH^- signals (likely the 1.2 ppm peak) originates from μ_3−OH^- close to the defects. The possible configurations of local structure are shown in Figure S11. Reintroducing water molecules into UiO-66-TFA-act200 results in a dominant ^1H signal at 3.9 ppm from H_2O and the disappearance of the μ_3−OH^- signal at 2.4 ppm (Figure 2b), which may be due to the μ_3−OH^- groups

https://doi.org/10.1021/jacs.5c13805
J. Am. Chem. Soc. 2025, 147, 44200−44215

Scheme 3. Schematic Illustration of the Structural Evolution of UiO-66 under Different Treatment Conditions Investigated in This Study[a]

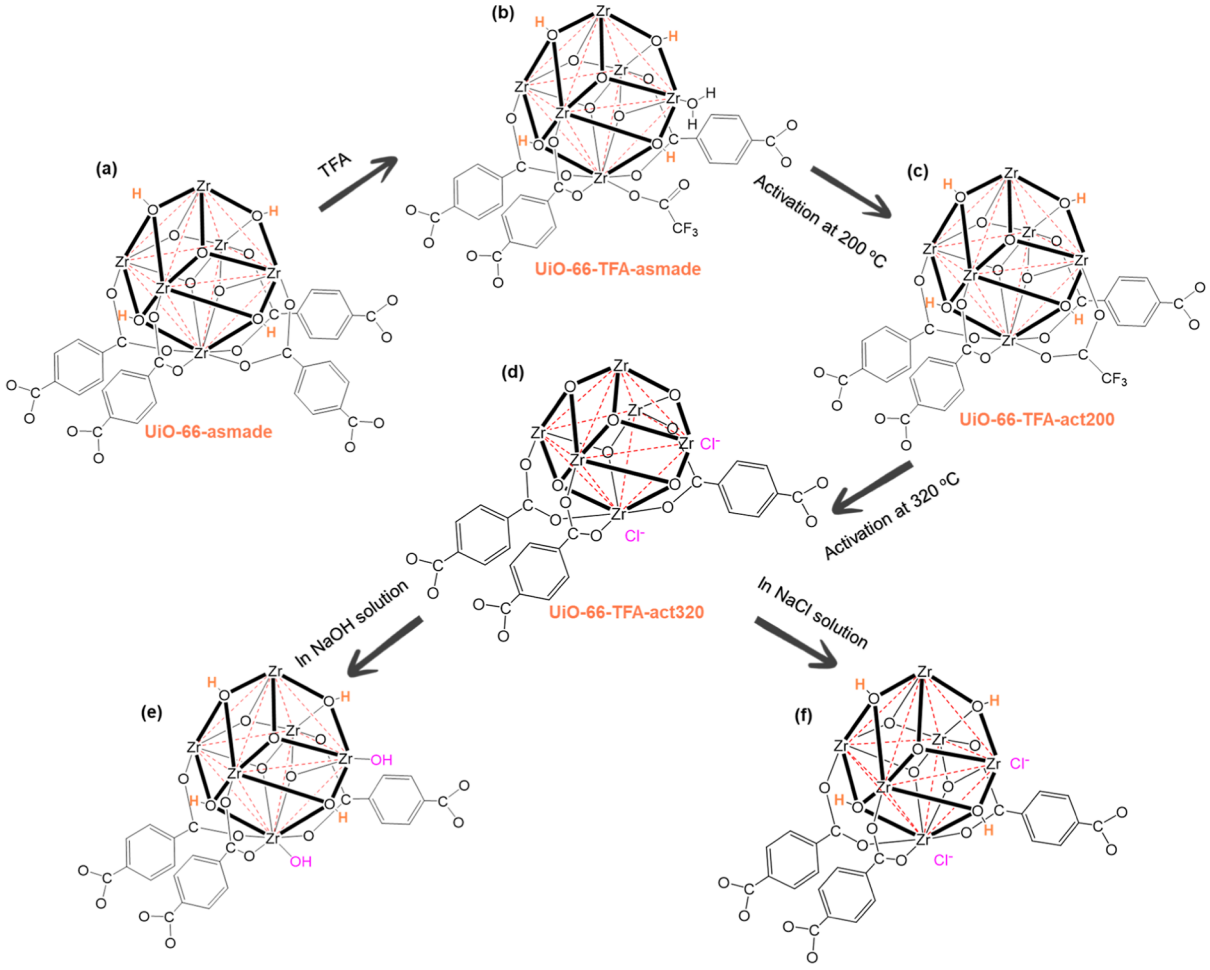

[a]For clarity, only the bottom Zr^{4+} site is shown with all its coordinated species. (a) In UiO-66-asmade, Zr^{4+} is coordinated by two μ_3−OH^-, two μ_3−O^{2-}, and four BDC linkers. (b) In UiO-66-TFA-asmade, Zr^{4+} is coordinated by two μ_3−OH^-, two μ_3−O^{2-}, three BDC linkers, and one TFA or one water molecule. (c) In UiO-66-TFA-act200, Zr^{4+} is coordinated by two μ_3−OH^-, two μ_3−O^{2-}, three BDC linkers, and one TFA. (d) In UiO-66-TFA-act320, Zr^{4+} is coordinated by approximately three μ_3−O^{2-} and three BDC linkers, with one Cl^- electrostatically associated. (e) After ion exchange in NaOH, Zr^{4+} is coordinated by two μ_3−OH^-, two μ_3−O^{2-}, three BDC linkers, and one OH^-. (f) After ion exchange in NaCl, Zr^{4+} is coordinated by two μ_3−OH^-, two μ_3−O^{2-}, and three BDC linkers, with one Cl^- electrostatically associated.

forming hydrogen bonds with water, causing the signal to become more deshielded and, therefore, be buried underneath the broad water resonance.[33] When the sample is reheated at 100 °C under vacuum, water molecules are removed and the μ_3−OH^- signal at 2.4 ppm reappears. Corresponding ^{19}F MAS NMR spectra collected during this water adsorption and desorption cycle (Figure 2c) show peak shifts between −81.4 and −77.0 ppm, further validating our proposed model of structural evolution (Scheme 2) with greater confidence.

To further explore the interaction/correlation between various proton-containing species, 2D ^1H−^1H SQ−SQ experiments were carried out using the three-pulse NOESY sequence. A representative spectrum with a mixing time of 100 ms is shown in Figure 2d. Cross-peaks at 1.2 and 2.4 ppm suggest close-spatial proximity between two inequivalent μ_3−OH^- groups in UiO-66-TFA-act200. In addition, cross peaks between μ_3−OH^- protons and aromatic protons suggest that they are also in close proximity. To further investigate short-range correlations, a 2D ^1H−^1H DQ−SQ experiment was performed using the Back-to-Back (BABA) recoupling sequence with one rotor period (20 μs) each for excitation and reconversion. While both methods rely on ^1H−^1H dipolar couplings to probe through-space proximities between protons, DQ−SQ experiment is more sensitive to short-range interactions.[49−52] In the DQ−SQ spectrum of UiO-66-TFA-act200 (Figure 2e), diagonal autocorrelation peaks at 7.8, 2.4, and 1.2 ppm along the SQ dimension validate close spatial proximity between protons of the same kind. However, two pairs of off-diagonal correlation peaks reveal that two types of μ_3−OH^- are in the vicinity of aromatic protons of BDC ligands, analogous to the observations in Figure 2d. In contrast, the spectrum of defect-free UiO-66-act200 (Figure S12) shows no such cross-peaks at the same contour intensity, suggesting a larger distance between μ_3−OH^- and the benzene rings. In the ^{17}O MAS spectrum of UiO-66-TFA-act200 (Figure 3a), the intensity of the μ_3−OH^- resonances decrease and move to lower chemical shift direction, likely due to the removal of water molecules that are initially hydrogen-bonded to μ_3−OH^- in UiO-66-TFA-asmade.

https://doi.org/10.1021/jacs.5c13805
J. Am. Chem. Soc. 2025, 147, 44200−44215

Overall, after activation at 200 °C, all residual solvent molecules are removed. The coordinated water is also eliminated, allowing the monodentate TFA to transform into a bidentate state bridging two adjacent Zr^{4+} sites (Scheme 3, from b to c). This change in coordination mode can be reversed upon reintroduction of water molecules.

Local Structure of Dehydroxylated UiO-66-TFA-act320. Further activation at 320 °C leads to the complete removal of terminal TFA molecules, as evidenced by the disappearance of the small peak at 164 ppm in $^{1}H-^{13}C$ CP MAS spectra (Figure 1a). Simultaneously, the absence of ^{19}F signals in the corresponding spectrum confirms total TFA removal and vacancy formation (Figure 1c). In addition, no μ_3-OH^- signal is observed in ^{17}O MAS spectra (Figure 3a), indicating complete dehydroxylation of the Zr clusters. Note that the spectral quality of UiO-66-TFA-act320 and UiO-66-act320 deteriorates due to the reduced ^{17}O content, likely resulting from isotopic exchange with non ^{17}O-labeled species or from dehydroxylation process. Nevertheless, the completion of dehydroxylation process is unambiguously confirmed by the disappearance of all proton signals except those from aromatic species in the ^{1}H MAS NMR spectra (Figure 2b). Both 2D DQ−SQ (Figure S12b) and SQ−SQ (Figure S13) spectra further support the absence of μ_3-OH^- groups. Importantly, the reversibility of structural transformations between $[Zr_6O_6]^{12+}$ and $[Zr_6O_4(OH)_4]^{12+}$ clusters is validated by the reappearance of μ_3-OH^- signals upon water exposure (Figure 2b). In addition, fitting the ^{17}O MAS NMR spectra of UiO-66-TFA-asmade and UiO-66-TFA-act320 (Figure S14 and Table S3) revealed a larger C_Q value of carboxylate oxygen for UiO-66-TFA-act320 (7.2 MHz) compared to UiO-66-TFA-asmade (6.2 MHz). This increase in C_Q indicates that dehydroxylation induces greater distortion of the Zr_6O_6 clusters, which is consistent with the XAFS results (see below).

To investigate the species responsible for charge balance following TFA removal, likely limited to OH^- or Cl^-, ion exchange was performed. UiO-66-TFA-act320 was first immersed in a 0.01 M NaOH solution and stirred at room temperature for 1 day, with the expectation that OH^- can be incorporated at the defect sites. The XRD pattern of the NaOH-treated material indicates that the framework structure is largely preserved, with only slight peak broadening suggesting some loss of crystallinity (Figure S15). The BET surface area of the MOF after NaOH treatment shows a relatively small decrease, from 865 to 763 $m^2\ g^{-1}$, indicating that no significant number of new defects were generated (Figure S16).

After treatment, a new ^{1}H MAS NMR peak appears at approximately −0.4 ppm (Figure S17a), which, therefore, can be assigned to isolated μ_1-OH^- species directly coordinated to Zr^{4+} vacant sites. This assignment is further supported by the emergence of a new IR band at 3625 cm^{-1} (Figure S18), consistent with calculated results that show several OH^- signals, with μ_1-OH^- appearing at lower frequencies relative to μ_3-OH^-.[53,54] These results rule out OH^- as the primary charge-balancing species. If OH^- were already present as the primary termination species immediately after TFA removal, then the μ_1-OH^- signal (at −0.2 ppm) should have been detected in the original UiO-66-TFA-act320 sample before any NaOH treatment or other postsynthetic steps. The results also indicate that OH^- groups can be introduced through ion exchange if needed for specific applications.

Given that OH^- groups are likely not the inherent charge-compensating species after TFA removal, the most plausible candidates are Cl^- ions derived from the hydrolysis of the $ZrCl_4$ precursor, considering the absence of other anionic species.

^{35}Cl SSNMR experiments were conducted to investigate the potential role of Cl^- in charge compensation. Unfortunately, no detectable ^{35}Cl signal is observed in the defective UiO-66 samples. This is due to ^{35}Cl being an unreceptive quadrupolar nucleus with a small γ and moderate natural abundance. Furthermore, the Cl content in the sample is very low (<0.3 wt %), as evidenced by EDS (Table S4). However, XAS is more sensitive and can detect elements with very low concentrations. Cl K-edge XANES spectra (Figure S19) confirm the presence of Cl^- across all UiO-66-TFA samples and reveal local environments different from that of the $ZrCl_4$ precursor, indicating that the detected Cl^- is not from residual unreacted $ZrCl_4$. Moreover, the Cl K-edge spectra of UiO-66-TFA-asmade and UiO-66-TFA-act200 are similar, while significant spectral changes are observed for UiO-66-TFA-act320. This indicates that Cl^- ions may undergo spatial redistribution after TFA removal in UiO-66-TFA-act320. The evolution of the local Cl^- environment is consistent with the hypothesis that exposed Zr^{4+} sites are neutralized by Cl^- ions, serving as charge-compensating species in the absence of coordinated modulators. We further conducted ion exchange experiments using saturated NaCl solution to enhance the Cl^- content (up to 7 wt %) (Table S4) at the defective Zr^{4+} sites in UiO-66-TFA-act320. The ion-exchanged sample was first washed with water several times and the corresponding XRD result shows no structural degradation after NaCl solution treatment, although some residual solid NaCl is present (Figure S15). In the resulting ^{35}Cl MAS NMR spectrum (Figure S17b), a main sharp peak at −47 ppm corresponds to NaCl crystals remaining in the MOF, while a weak, broad signal near 0 ppm indicates Cl^- ions that are randomly distributed in the MOF pores. We also measured ^{37}Cl MAS NMR spectrum (Figure S17c), which mirrors ^{35}Cl results. Typically, Cl^- directly coordinated to Zr^{4+} in other systems exhibits isotropic chemical shift in the range of several hundred (200−400) ppm.[55−59] Therefore, the absence of such signals in our spectra suggests that Cl^- does not directly coordinate to Zr^{4+} in a well-defined manner (speculated as μ_3-Cl^- or μ_1-Cl^-). Instead, Cl^- may remain electrostatically associated near the vacant Zr^{4+} sites to maintain charge balance, without forming strong coordination bonds. The post-treatment of UiO-66-TFA-act320 with NaCl also leads to a partial, if not complete, reversion of the $[Zr_6O_6]^{12+}$ clusters back to the $[Zr_6O_4(OH)_{4-x}Cl_x]^{12+}$ composition due to the presence of water in the NaCl solution. This is corroborated by the reappearance of μ_3-OH^- signals in the ^{1}H MAS spectra (Figure S17a).

Overall, activation at 320 °C induces both dehydroxylation of the $[Zr_6O_4(OH)_4]^{12+}$ cluster to $[Zr_6O_6]^{12+}$ and the removal of coordinated TFA molecules (Scheme 3, from c to d). While we cannot completely rule out direct Zr−Cl coordination, the combined absence of distinct signals in the direct Zr−Cl region and the presence of a broad resonance around 0 ppm support the view that chloride is predominantly present in an electrostatically associated state (i.e., as charge-compensating species residing within the MOF pores) (Scheme 3, from d to f). On the other hand, terminal μ_1-OH^- groups can be introduced through ion exchange in NaOH solution (Scheme

https://doi.org/10.1021/jacs.5c13805
J. Am. Chem. Soc. 2025, 147, 44200−44215

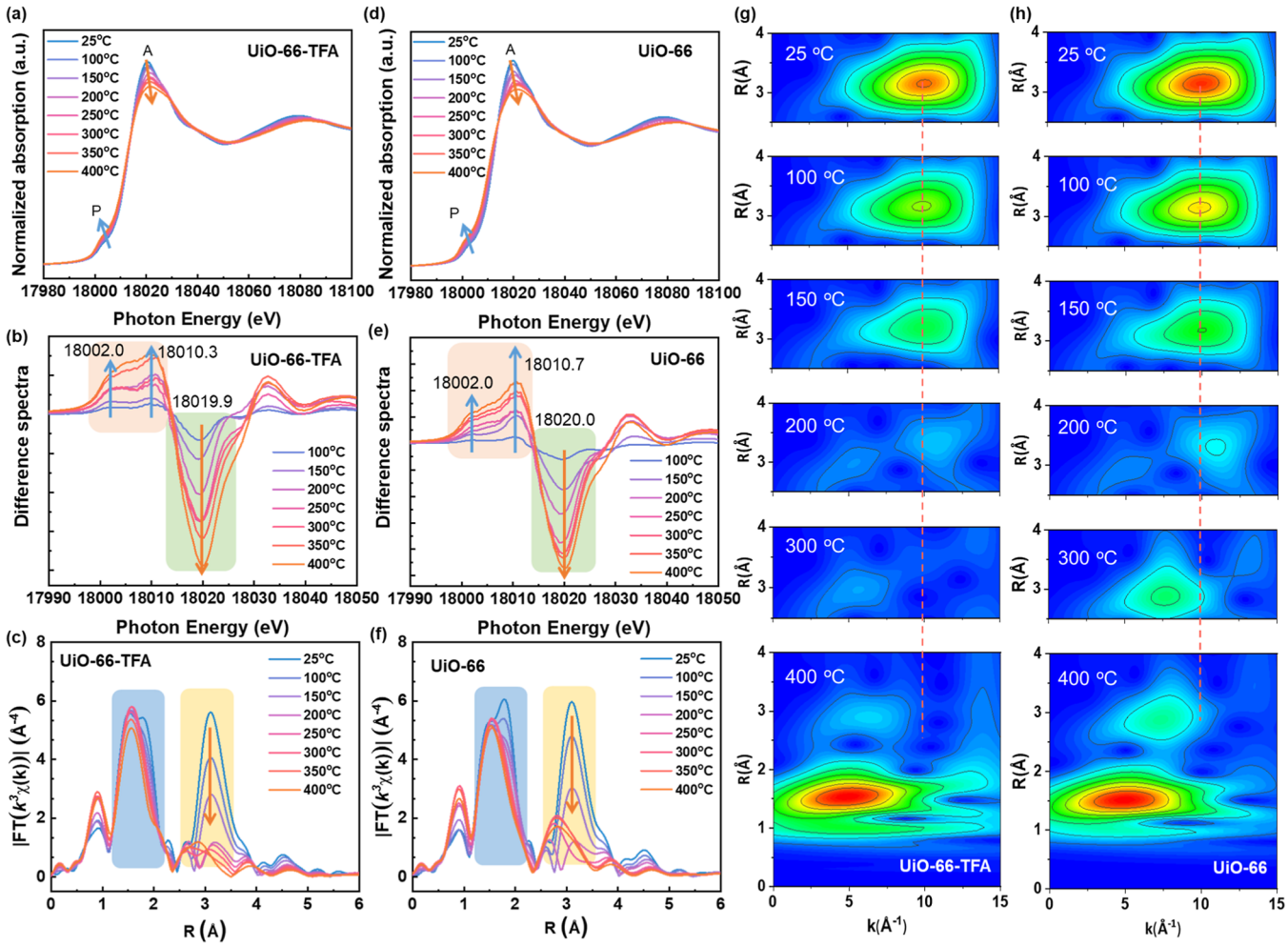

Figure 4. In situ Zr K-edge XANES spectra of (a) UiO-66-TFA and (d) UiO-66 recorded at temperatures ranging from 25 to 400 °C. (b,e) The corresponding difference spectra, obtained by subtracting the spectrum at 25 °C from those at higher temperatures, showing spectral changes during the heating process. The reddish and greenish regions represent the pre-edge and main adsorption peak, respectively. (c,f) The corresponding Fourier-transformed EXAFS spectra. (g,h) The corresponding wavelet transform of the k^3 weighted EXAFS data.

3, from d to e). These post-treatments provide an effective strategy to tailor the local coordination environment of defective UiO-66.

XAFS for Local Environment of Zr. Wideline ^{91}Zr SSNMR has proven effective in revealing local structural environments around Zr centers in MOFs including UiO-66.[37,38,58,60,61] However, our recent work shows that directly probing defective Zr sites remains highly challenging due to the isotope's inherently low natural abundance, low gyromagnetic ratio, and relatively large quadrupolar moment. These unfavorable NMR properties are further compounded by the low concentration of defects and significantly reduced spherical symmetry at defective Zr sites, leading to extremely broad spectra and poor sensitivity. As a result, the observation of defective Zr is extremely difficult, if not impossible, even at ultrahigh magnetic fields (e.g., 36 T).

Therefore, in this work, in situ heating XAFS experiments are conducted to give more details about the local structure evolution of defective Zr clusters during the activation process. This technique enables real-time tracking of coordination changes, such as dehydroxylation and TFA removal, under thermal treatment. Remarkable changes are observed in the X-ray absorption near-edge structure (XANES) spectra at Zr K-edges (Figure 4a,d). Both defect-free and defective UiO-66 display the increased pre-edge peak (P) intensity and the reduced white-line peak (A) intensity with rising temperature. The pre-edge peak corresponds to the electron transition from 1s to 4d, which is typically forbidden but becomes allowed due to mixing between Zr 4d and O 2p orbitals. The increased intensity of this peak suggests enhanced d-p orbital mixing, representing a greater distortion from centrosymmetry induced by dehydroxylation.[62,63] This means that during this process, the original $Zr_6O_4(OH)_4$ octahedron gradually evolves into a distorted Zr_6O_6 octahedron.[7] The disappearance of bridging OH^- bonds in Fourier-transform infrared (FTIR) spectra after activation at 320 °C further proves the successful dehydroxylation (Figure S18). To better visualize these spectral changes, difference spectra were obtained by subtracting the 25 °C spectrum from those at higher temperatures, as shown in Figure 4b,e. For both samples, the split peaks at ~18002.0 and 18010.3 eV in the pre-edge region (reddish area) become more intense, likely originating from the splitting of e_g (d_{z^2}, $d_{x^2-y^2}$) and t_{2g} (d_{xy}, d_{xz}, d_{yz}) orbitals due to gradual structural distortion. Meanwhile, the main peak (greenish area) at ~18019.9 eV gradually decreases, indicating the loss of coordinated O atoms during the dehydroxylation process.[7]

https://doi.org/10.1021/jacs.5c13805
J. Am. Chem. Soc. 2025, 147, 44200−44215

Scheme 4. Schematic Illustration of the Coordination Environment Evolution of Metal Clusters in (a) UiO-66-TFA and (b) UiO-66[a]

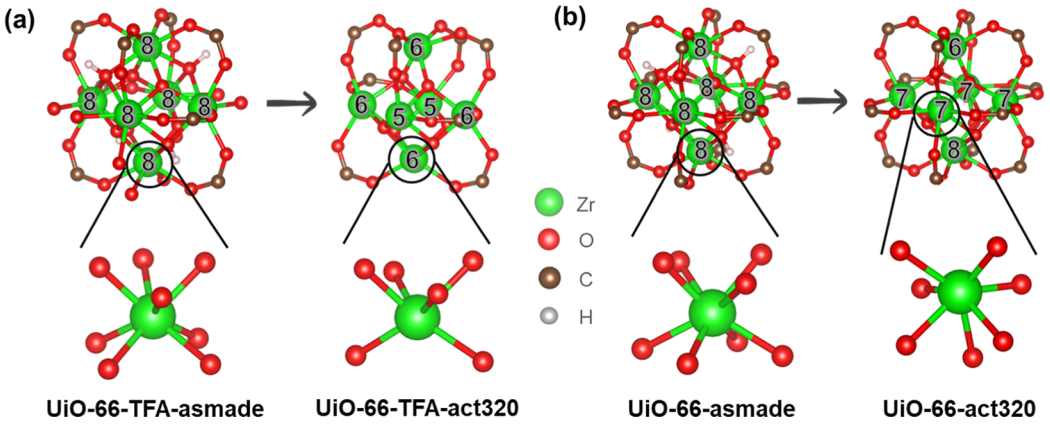

[a]For clarity, the full structures of linkers are not shown. BDC represented as O−C−O, and the TFA/H_2O pair is depicted as dangling O atoms. The numbers indicate the Zr−O coordination number at each metal site. The bottom figures show an enlarged view of a single Zr site.

Although the overall spectral trends are similar for both samples, notable differences emerge upon Fourier transforming the XAFS data from *k*-space to *R*-space (without phase correction). In Figure 4c,f, two primary peaks are observed: one at 1.0−2.2 Å (blue region), corresponding to Zr−O scattering in the first shell, and another at 2.7−3.5 Å (yellow region), attributed to Zr−Zr scattering in the second shell. It is noted that at the beginning of the heating process, a peak splitting exists in the first coordination shell, which eventually merges into a single peak with a shorter average bond length. In the ideal UiO-66 (pristine) structure, each Zr is coordinated by eight oxygen atoms that can be classified into two types based on the bond distances, i.e. two μ_3−O^{2-} bridging bonded to three Zr atoms with short Zr−O bonds and other six O atoms from μ_3−OH^- and BDC with ∼0.14 Å longer Zr−O bonds.[7,64] Therefore, it is deduced that the split peaks are due to oxygen atoms at two distinct bond distances. The intensity ratio of these two peaks differs between UiO-66-TFA and UiO-66, which may be influenced by variations in Zr−O paths induced by the coordinated TFA. Upon heating, as μ_3−OH^- groups are removed and Zr−O distances decrease, the Zr_6O_6 clusters, therefore, become increasingly distorted. In terms of UiO-66-TFA, the loss of TFA is expected to further affect the local Zr coordination environment. To verify these changes, a model of UiO-66-TFA after dehydroxylation was constructed and optimized, assuming Zr sites remain vacant (Figure S20a). The calculated XANES spectrum produced by Feff9 (Figure S20b) closely matches the experimental spectrum, supporting the reliability of the proposed structure.

To quantitatively determine the local Zr coordination environment, EXAFS fittings were performed on UiO-66-TFA at room temperature and at 400 °C using the predicted structure. The results are presented in Table S5 and Figure S21. The overall average Zr−O coordination number in the first shell decreases from 8 to 6 due to the loss of ligands and μ_3−OH^- groups. An illustration reflecting the coordination environment evolution is shown in Scheme 4. Additionally, the average Zr−O bond distance shortens by approximately 0.05 Å, confirming the shrinkage of Zr_6O_6 clusters. Consistent with previous results for defect-free UiO-66,[7] two Zr−Zr paths with distinct distances appear in the second shell, with one elongated and the other shortened, reflecting a unidirectional compression of Zr_6O_6 clusters. This distortion may cause the cancellation of backscattering wave interference;[65] thus, in the *k*-space (Figure S22), the amplitude of the high *k* region, corresponding to Zr−Zr interactions, gradually decreases with increasing temperature, which also contributes to the weakened second-shell peak in *R* space. Wavelet transform (WT) data of the EXAFS region further corroborate these findings. As shown in Figure 4g,h, the contour peak at k = 10 $Å^{-1}$ and R = 3.1 Å, associated with Zr−Zr coordination, gradually diminishes with increasing temperature. Another obvious finding is that although both samples exhibit a left-shifted second-shell peak (indicating a decrease in the averaged Zr−Zr distance), the peak intensity in UiO-66-TFA is weaker than that in defect-free UiO-66. This further confirms that the removal of TFA induces dramatic distortion in the Zr_6O_6 cluster.

HER Performance of Pt NPs Loaded UiO-66. To exploit the effect on catalysis of the defects in UiO-66 introduced in this study, we incorporated Pt NPs into the system and evaluated their performance in HER. By adding a small amount of aqueous H_2PtCl_6 solution during the synthesis of UiO-66, Pt-loaded samples with and without defects were prepared. XRD results confirm the crystal structure of UiO-66 remains intact (Figure S23), with no sign of Pt and/or PtO_2 phases. However, the Pt L_3-edge XANES spectrum of Pt-UiO-66-TFA-act320 (Figure S24) is similar to that of Pt foil, while its corresponding *k*-space and *R*-space features show weakened intensity of Pt−Pt coordination. These results suggest the presence of metallic Pt in the form of small NPs, which is undetectable by XRD due to their small size or low concentration (0.17 and 0.12 wt % for Pt-UiO-66-TFA-act320 and Pt-UiO-66-act320, respectively, as determined by ICP). XPS further confirms the Pt-oxidation state, showing a Pt^0 signal despite the low signal-to-noise ratio (Figure S25). Although several reports have presented ^{195}Pt SSNMR studies on Pt-loaded samples, the Pt content in those cases is relativity high (over 3 wt %).[66−69] More recently, ^{195}Pt SSNMR has been applied to probe the coordination environment of Pt single atoms with Pt loadings as low as 1 wt %.[70] However, such measurements still require prolonged time to acquire spectra with meaningful S/N ratio. Therefore, ^{195}Pt SSNMR measurements are impractical in this work due to the very low Pt loading (i.e., 0.17% or lower).

https://doi.org/10.1021/jacs.5c13805
J. Am. Chem. Soc. 2025, 147, 44200−44215

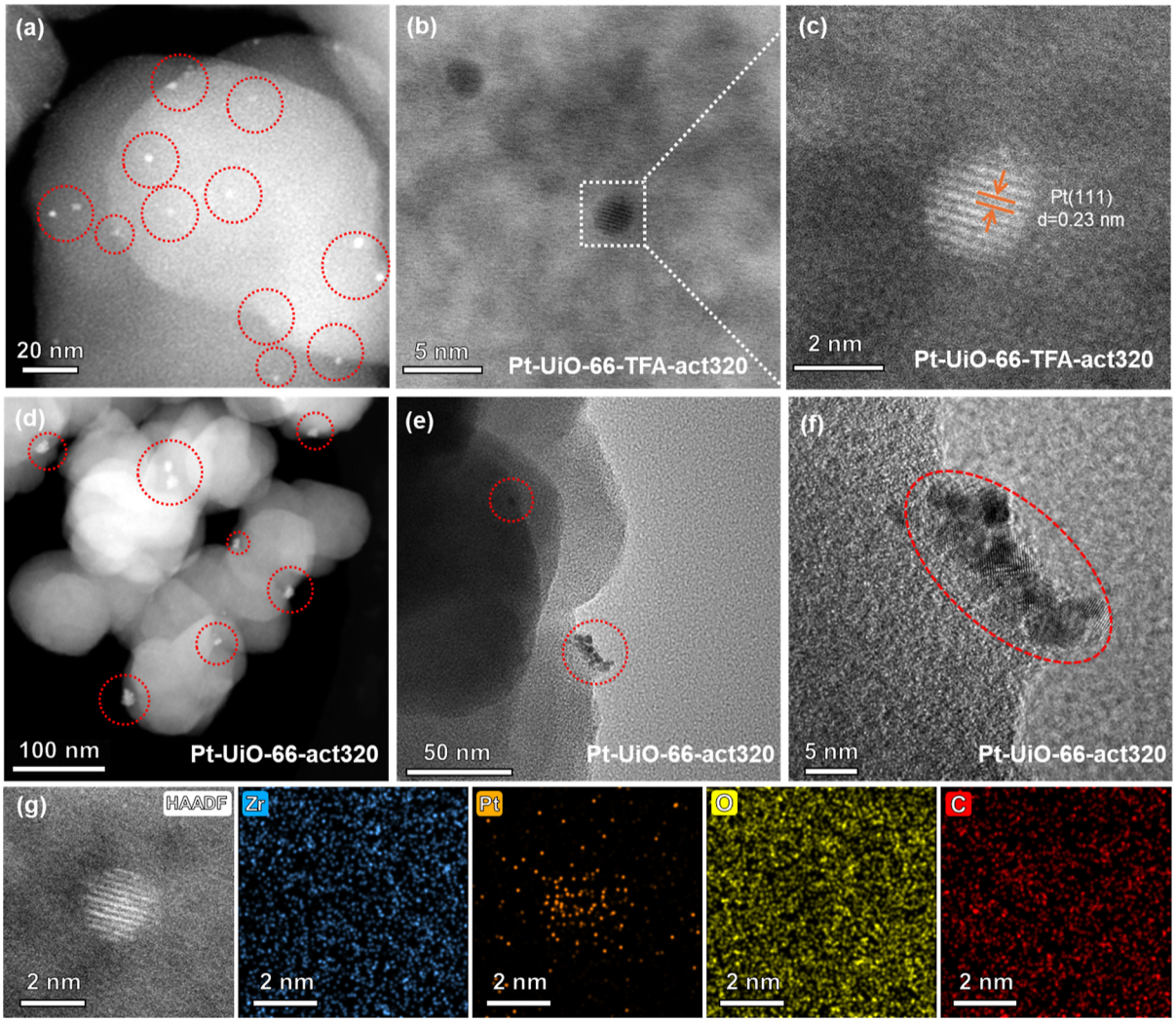

Figure 5. HAADF-STEM image, TEM image, and HRTEM image of (a–c) Pt-UiO-66-TFA-act320 and (d–f) Pt-UiO-66-act320. The red circles highlight the dispersed Pt nanoparticles. (g) HAADF-STEM image and elemental mapping images of Pt-UiO-66-TFA-act320 (Zr: blue, Pt: orange, O: yellow and C: red).

To directly visualize Pt NPs, we employed transmission electron microscope (TEM) and high-angle-annular-dark-field scanning transmission electron microscopy (HAADF-STEM). As shown in the HAADF-STEM images (Figure 5a,d), bright spots, marked with red dashed circles, correspond to Pt NPs embedded in the UiO-66 matrix. High-magnification TEM images (Figure 5b,e) reveal that Pt NPs are highly aggregated in the defect-free UiO-66 (Pt-UiO-66-act320), while they are more uniformly distributed in the defective UiO-66 (Pt-UiO-66-TFA-act320). The average size of Pt NPs in Pt-UiO-66-TFA-act320 is ∼1.9 nm (Figure S26), which aligns with the cage diameter of missing cluster defects, whereas the aggregated Pt NPs in Pt-UiO-66-act320 exceed 10 nm (Figure 5f). High-resolution imaging also resolves clear lattice fringes with an interplanar spacing of 0.23 nm, characteristic of Pt (111) facets (Figure 5c). EDS mapping further confirms the homogeneous distribution of Zr, O, and C in Pt-UiO-66-TFA-act320 at the large scale (Figure S27). At higher magnification, EDS presents a rough outline of the Pt NPs within the framework (Figure 5g). In contrast, for Pt-UiO-66-act320, the EDS maps clearly reveal the presence of large Pt NPs aggregates (Figure S28). These findings may indicate that in the defective UiO-66, Pt precursors are preferentially anchored at defect sites, where they subsequently form Pt NPs, as shown in Scheme S1. The confined environment of the defects limits further particle growth. In contrast, in the absence of defects, Pt lacks anchoring sites and tends to aggregate into larger particles outside the pores of the MOF.

The HER performance of the samples was evaluated using a standard three-electrode setup in N_2-saturated 0.5 M H_2SO_4 at room temperature. As shown by linear sweep voltammetry (LSV) curves (Figure 6a), Pt-UiO-66-TFA-act320 presents a much lower overpotential of 80 mV compared to 192 mV for Pt-UiO-66-act320 at a current density of −10 mA cm^{-2} (see the inset figure). Although it does not exceed the overpotential of commercial 20 wt % Pt/C catalyst (28 mV), the mass activity of Pt-UiO-66-TFA-act320 reaches 8.4 A mg_{Pt}^{-1}, which is 21 times higher than that of Pt/C[71,72] and ∼8 times higher than that of Pt-UiO-66-act320 (Figure 6b). Meanwhile, the corresponding Tafel slope (Figure 6c) of Pt-UiO-66-TFA-act320 (66 mV dec^{-1}) is significantly lower than that of Pt-UiO-66-act320 (113 mV dec^{-1}), UiO-66-TFA-act320 (270 mV dec^{-1}) and UiO-66-act320 (279 mV dec^{-1}), indicating more favorable HER kinetics. Note that without Pt NPs, UiO-66 alone exhibits minimal HER activity, although defective UiO-66-TFA shows slightly enhanced performance, suggesting

https://doi.org/10.1021/jacs.5c13805
J. Am. Chem. Soc. 2025, 147, 44200−44215

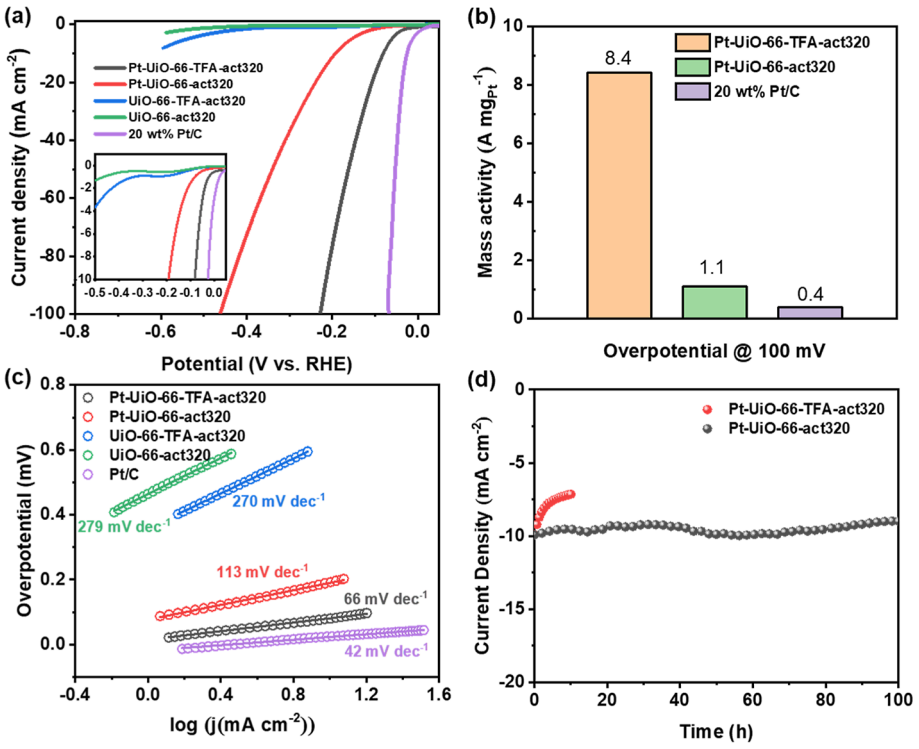

Figure 6. (a) LSV curves of Pt-UiO-66-TFA-act320, Pt-UiO-66-act320, UiO-66-TFA-act320, UiO-66-act320, and commercial 20 wt % Pt/C for HER in 0.5 M H_2SO_4 at room temperature. The inset enlarged figure compares the overpotential required to obtain a current density of 10 mA cm^{-2}. (b) Mass activity of Pt-UiO-66-TFA-act320, Pt-UiO-66-act320, and commercial Pt/C at the overpotential of 100 mV. (c) Tafel slope acquired from corresponding LSV curves. (d) Chronoamperometry curves of Pt-UiO-66-TFA-act320 and Pt-UiO-66-act320 recorded at their respective fixed overpotential to obtain 10 mA cm^{-2}.

that Pt serve as the active sites while UiO-66 mainly works as a support material. Moreover, the intrinsic activity of the Pt NPs was further assessed via electrochemical active surface area (ECSA), estimated from double-layer capacitance (C_{dl}). As shown in Figure S29, the higher C_{dl} value for Pt-UiO-66-TFA-act320 compared to Pt-UiO-66-act320 indicates a larger accessible surface area and improved catalytic activity. Electrochemical impedance spectroscopy (EIS) (Figure S30) was used to study interfacial charge transfer resistance. Fitting the EIS data allows for the determination of solution resistance (R_s) and charge transfer resistance (R_{ct}) (Table S6). The results show Pt-UiO-66-TFA-act320 has the lowest R_{ct} value among all samples, indicating the fastest electron transfer kinetics and superior HER performance. Finally, the stability was evaluated via chronoamperometry tests (Figure 6d). Pt-UiO-66-TFA-act320 maintains a current density of 10 mA cm^{-2} for over 100 h with minimal activity loss, while Pt-UiO-66-act320 experiences a ~25% decrease in current density within the first 4 h. These results demonstrate that while the MOF porous structure ensures the accessibility of Pt NPs, the confinement effect of defects effectively suppresses their aggregation, thereby enhancing both catalytic efficiency and durability.

CONCLUSION

In summary, we have used various SSNMR techniques combined with XAS to elucidate the local structure and evolution of defects in UiO-66. By choosing TFA as a modulator, both missing-linker and missing-cluster defects are introduced into UiO-66. We found that the local structures of these defects undergo distinct structural transformations depending on the treatment conditions (pristine, desolvated, and dehydroxylated states) through various SSNMR methods. Specifically, we conducted ^{1}H, ^{13}C, ^{19}F, ^{17}O, and $^{35/37}Cl$ MAS, $^{1}H-^{13}C$ CP, $^{19}F-^{13}C$ CP, ^{17}O 3QMAS, ^{1}H DQ–SQ and ^{1}H SQ–SQ experiments, which enabled us to follow the structural evolution of local environments around defects, identify various defect-associated species and monitor their behavior during various postsynthetic treatments.

In particular, ^{1}H and ^{19}F MAS spectra confirm that H_2O and the deprotonated TFA modulator initially occupy adjacent two Zr^{4+} defect sites. After thermal activation at 200 °C, H_2O is removed, and the dangling TFA on one Zr^{4+} site transforms into bidentate coordination with one pair of Zr^{4+} sites. Further heating to 320 °C induces dehydroxylation and the complete removal of TFA, generating vacant and unsaturated Zr^{4+} sites. Furthermore, to investigate potential charge-compensating species in the system, ion-exchange experiments were conducted in NaOH and NaCl solutions, respectively. ^{1}H and $^{35/37}Cl$ SSNMR reveal that Cl^- ions act as charge-compensating species but do not directly coordinate to the vacant Zr^{4+} sites. In contrast, terminal μ_1-OH^- groups can be introduced through postsynthetic modification with NaOH.

In situ X-ray absorption fine structure (XAFS) experiments confirm the dehydroxylation process, revealing a progressive decrease in the average Zr–O coordination number and a reduction in Zr–O bond lengths, indicative of μ_3-OH^- group removal and cluster distortion at elevated temperatures.

Capitalizing on the abundant defect sites, we employed UiO-66-TFA-act320 as a functional support for the deposition of Pt nanoparticles (NPs). High-angle annular dark-field scanning transmission electron microscopy (HAADF-STEM) and

https://doi.org/10.1021/jacs.5c13805
J. Am. Chem. Soc. 2025, 147, 44200–44215

elemental mapping confirm the uniform distribution of small Pt NPs throughout the MOF matrix. The confinement effect provided by the defect-rich regions effectively anchors the Pt NPs, suppressing aggregation and enabling high dispersion. The Pt-loaded defective UiO-66 was evaluated for hydrogen evolution reaction (HER) performance under acidic conditions. Compared to its defect-free counterpart, the defective catalyst exhibits enhanced catalytic activity and superior stability. These findings demonstrate the crucial role of defects in stabilizing Pt NPs and preventing their aggregation.

Overall, we provide a comprehensive characterization of defects in UiO-66 by integrating complementary techniques, including SSNMR, XAFS, XRD, TGA, FT-IR, HAADF-STEM, and BET. While each method alone offers only a partial perspective, their combined application enables a coherent picture that bridges molecular-level chemical information with atomic-scale structural insights. This integrated approach clarifies how defects evolve and influence framework stability and functionality. Because defective UiO-66 represents one of the most well-known challenges in the field, achieving a clearer picture of its defect structures has significant implications for defect engineering. Beyond UiO-66, our findings highlight the broader importance of multitechnique strategies for investigating complex defect chemistries in MOFs. Such insights not only deepen the fundamental understanding of defect structures but also provide a foundation for the rational design and defect engineering of MOFs for targeted applications in catalysis, adsorption, and energy-related processes.

■ ASSOCIATED CONTENT

Supporting Information

The Supporting Information is available free of charge at https://pubs.acs.org/doi/10.1021/jacs.5c13805.

Experimental details and additional characterization (TGA, XRD, XPS, FT-IR, TOF-SIMS, XANES, BET isotherms, NMR data, EXAFS fitting, TEM mapping, electrochemical tests, and Feff calculation) (PDF)

■ AUTHOR INFORMATION

Corresponding Authors

Jun Zhong − *Institute of Functional Nano and Soft Materials Laboratory (FUNSOM), Jiangsu Key Laboratory for Carbon-Based Functional Materials & Devices, Soochow University, Suzhou 215123, China;* orcid.org/0000-0002-8768-1843; Email: jzhong@suda.edu.cn

Tsun-Kong Sham − *Department of Chemistry, The University of Western Ontario, London, Ontario N6A 5B7, Canada;* orcid.org/0000-0003-1928-6697; Email: tsham@uwo.ca

Yining Huang − *Department of Chemistry, The University of Western Ontario, London, Ontario N6A 5B7, Canada;* orcid.org/0000-0001-9265-5896; Email: yhuang@uwo.ca

Authors

Jiabin Xu − *Department of Chemistry, The University of Western Ontario, London, Ontario N6A 5B7, Canada; Institute of Functional Nano and Soft Materials Laboratory (FUNSOM), Jiangsu Key Laboratory for Carbon-Based Functional Materials & Devices, Soochow University, Suzhou 215123, China;* orcid.org/0000-0002-9693-2261

Kun Feng − *Institute of Functional Nano and Soft Materials Laboratory (FUNSOM), Jiangsu Key Laboratory for Carbon-Based Functional Materials & Devices, Soochow University, Suzhou 215123, China*

Wanli Zhang − *Department of Chemistry, The University of Western Ontario, London, Ontario N6A 5B7, Canada*

Amrit Venkatesh − *National High Magnetic Field Laboratory, Tallahassee, Florida 32310, United States; Department of Chemistry, University of Virginia, Charlottesville, Virginia 22904, United States;* orcid.org/0000-0001-5319-9269

Ivan Hung − *National High Magnetic Field Laboratory, Tallahassee, Florida 32310, United States;* orcid.org/0000-0001-8916-739X

Yuzhen Liu − *Frontiers Science Center for Rare Isotopes, Lanzhou Magnetic Resonance Center, College of Chemistry and Chemical Engineering, Lanzhou University, Lanzhou 730000, China*

Jingyan Liu − *Department of Chemistry, The University of Western Ontario, London, Ontario N6A 5B7, Canada*

Shuting Li − *Department of Chemistry, The University of Western Ontario, London, Ontario N6A 5B7, Canada*

Giuliana Battiston − *Department of Chemistry, The University of Western Ontario, London, Ontario N6A 5B7, Canada*

Zhehong Gan − *National High Magnetic Field Laboratory, Tallahassee, Florida 32310, United States;* orcid.org/0000-0002-9855-5113

Shoushun Chen − *Frontiers Science Center for Rare Isotopes, Lanzhou Magnetic Resonance Center, College of Chemistry and Chemical Engineering, Lanzhou University, Lanzhou 730000, China;* orcid.org/0009-0009-4315-015X

Yun-Mui Yiu − *Department of Chemistry, The University of Western Ontario, London, Ontario N6A 5B7, Canada*

Complete contact information is available at: https://pubs.acs.org/10.1021/jacs.5c13805

Notes

The authors declare no competing financial interest.

■ ACKNOWLEDGMENTS

The authors acknowledge Dr. Mathew Willans of J.B. Stothers NMR Facility at Western University for the setup of SSNMR experiments and Ning Chen and Weifeng Chen of HXMA beamline at the Canadian Light Source for their assistance in situ XAFS measurements. Y.H. thanks the Natural Science and Engineering Research Council (NSERC) of Canada for a Discovery Grant. The National High Magnetic Field Laboratory is supported by the National Science Foundation through NSF/DMR-2128556, and the State of Florida. The magnet and NMR instrumentation were supported by the NIH (BTRR 1P41GM122698 and RM1GM148766). T.S. also thanks the Canada Research Chair (CRC), Canada Foundation for Innovation (CFI), and the University of Western Ontario (operating grant for the Soochow Western Centre for Synchrotron Radiation Research). Canadian Light Source is supported by CFI, NSERC, the National Research Council (NRC), the Canadian Institutes of Health Research (CIHR), the Government of Saskatchewan, and the University of Saskatchewan. The authors would like to sincerely thank Professor Aaron J. Rossini at Iowa State University for enlightening discussions.

REFERENCES

(1) Queisser, H. J.; Haller, E. E. Defects in semiconductors: some fatal, some vital. *Science* **1998**, *281*, 945−950.

(2) Alkauskas, A.; McCluskey, M. D.; Van de Walle, C. G. Tutorial: Defects in semiconductors-Combining experiment and theory. *J. Appl. Phys.* **2016**, *119*, 181101.

(3) Taddei, M. When defects turn into virtues: The curious case of zirconium-based metal-organic frameworks. *Coord. Chem. Rev.* **2017**, *343*, 1−24.

(4) Guillerm, V.; Eddaoudi, M. The Importance of Highly Connected Building Units in Reticular Chemistry: Thoughtful Design of Metal−Organic Frameworks. *Acc. Chem. Res.* **2021**, *54*, 3298−3312.

(5) Schaate, A.; Roy, P.; Godt, A.; Lippke, J.; Waltz, F.; Wiebcke, M.; Behrens, P. Modulated Synthesis of Zr-Based Metal−Organic Frameworks: From Nano to Single Crystals. *Chem.—Eur. J.* **2011**, *17*, 6643−6651.

(6) Cavka, J. H.; Jakobsen, S.; Olsbye, U.; Guillou, N.; Lamberti, C.; Bordiga, S.; Lillerud, K. P. A New Zirconium Inorganic Building Brick Forming Metal Organic Frameworks with Exceptional Stability. *J. Am. Chem. Soc.* **2008**, *130*, 13850−13851.

(7) Valenzano, L.; Civalleri, B.; Chavan, S.; Bordiga, S.; Nilsen, M. H.; Jakobsen, S.; Lillerud, K. P.; Lamberti, C. Disclosing the Complex Structure of UiO-66 Metal Organic Framework: A Synergic Combination of Experiment and Theory. *Chem. Mater.* **2011**, *23*, 1700−1718.

(8) Cox, C. S.; Slavich, E.; Macreadie, L. K.; McKemmish, L. K.; Lessio, M. Understanding the Role of Synthetic Parameters in the Defect Engineering of UiO-66: A Review and Meta-analysis. *Chem. Mater.* **2023**, *35*, 3057−3072.

(9) Shearer, G. C.; Chavan, S.; Bordiga, S.; Svelle, S.; Olsbye, U.; Lillerud, K. P. Defect Engineering: Tuning the Porosity and Composition of the Metal−Organic Framework UiO-66 via Modulated Synthesis. *Chem. Mater.* **2016**, *28*, 3749−3761.

(10) Feng, X.; Jena, H. S.; Krishnaraj, C.; Leus, K.; Wang, G.; Chen, H.; Jia, C.; Van Der Voort, P. Generating Catalytic Sites in UiO-66 through Defect Engineering. *ACS Appl. Mater. Interfaces* **2021**, *13*, 60715−60735.

(11) Cirujano, F. G.; Llabrés i Xamena, F. X. Tuning the Catalytic Properties of UiO-66 Metal-Organic Frameworks: From Lewis to Defect-Induced Bronsted Acidity. *J. Phys. Chem. Lett.* **2020**, *11*, 4879−4890.

(12) Wu, H.; Chua, Y. S.; Krungleviciute, V.; Tyagi, M.; Chen, P.; Yildirim, T.; Zhou, W. Unusual and Highly Tunable Missing-Linker Defects in Zirconium Metal−Organic Framework UiO-66 and Their Important Effects on Gas Adsorption. *J. Am. Chem. Soc.* **2013**, *135*, 10525−10532.

(13) Hayashi, S.; Hayamizu, K. Chemical Shift Standards in High-Resolution Solid-State NMR (1) ^{13}C, ^{29}Si, and ^{1}H Nuclei. *Bull. Chem. Soc. Jpn.* **1991**, *64*, 685−687.

(14) Lawrence, M. C.; Spoel, A. M.; Katz, M. J. Pore Perfection vs Defect Design: Examining the Complex Relationship between Pore Structure and Carbon Dioxide Adsorption in Zr-Based MOFs. *J. Phys. Chem. C* **2024**, *128*, 10698−10704.

(15) Liu, L.; Chen, Z.; Wang, J.; Zhang, D.; Zhu, Y.; Ling, S.; Huang, K. W.; Belmabkhout, Y.; Adil, K.; Zhang, Y.; Slater, B.; Eddaoudi, M.; Han, Y. Imaging defects and their evolution in a metal-organic framework at sub-unit-cell resolution. *Nat. Chem.* **2019**, *11*, 622−628.

(16) Sannes, D. K.; Øien-Ødegaard, S.; Aunan, E.; Nova, A.; Olsbye, U. Quantification of Linker Defects in UiO-Type Metal−Organic Frameworks. *Chem. Mater.* **2023**, *35*, 3793−3800.

(17) Feng, Y.; Chen, Q.; Jiang, M.; Yao, J. Tailoring the Properties of UiO-66 through Defect Engineering: A Review. *Ind. Eng. Chem. Res.* **2019**, *58*, 17646−17659.

(18) Feng, X.; Jena, H. S.; Krishnaraj, C.; Arenas-Esteban, D.; Leus, K.; Wang, G.; Sun, J.; Rüscher, M.; Timoshenko, J.; Roldan Cuenya, B.; Bals, S.; Voort, P. V. D. Creation of Exclusive Artificial Cluster Defects by Selective Metal Removal in the (Zn, Zr) Mixed-Metal UiO-66. *J. Am. Chem. Soc.* **2021**, *143*, 21511−21518.

(19) Tan, K.; Pandey, H.; Wang, H.; Velasco, E.; Wang, K. Y.; Zhou, H. C.; Li, J.; Thonhauser, T. Defect Termination in the UiO-66 Family of Metal-Organic Frameworks: The Role of Water and Modulator. *J. Am. Chem. Soc.* **2021**, *143*, 6328−6332.

(20) Taddei, M.; Wakeham, R. J.; Koutsianos, A.; Andreoli, E.; Barron, A. R. Post-Synthetic Ligand Exchange in Zirconium-Based Metal−Organic Frameworks: Beware of The Defects. *Angew. Chem., Int. Ed.* **2018**, *57*, 11706−11710.

(21) Devulapalli, V. S. D.; McDonnell, R. P.; Ruffley, J. P.; Shukla, P. B.; Luo, T.-Y.; De Souza, M. L.; Das, P.; Rosi, N. L.; Karl Johnson, J.; Borguet, E. Identifying UiO-67 Metal-Organic Framework Defects and Binding Sites through Ammonia Adsorption. *ChemSusChem* **2022**, *15*, No. e202102217.

(22) Trickett, C. A.; Gagnon, K. J.; Lee, S.; Gándara, F.; Bürgi, H. B.; Yaghi, O. M. Definitive Molecular Level Characterization of Defects in UiO-66 Crystals. *Angew. Chem., Int. Ed.* **2015**, *54*, 11162−11167.

(23) Shearer, G. C.; Chavan, S.; Ethiraj, J.; Vitillo, J. G.; Svelle, S.; Olsbye, U.; Lamberti, C.; Bordiga, S.; Lillerud, K. P. Tuned to Perfection: Ironing Out the Defects in Metal−Organic Framework UiO-66. *Chem. Mater.* **2014**, *26*, 4068−4071.

(24) Zhao, H.; Yi, B.; Si, X.; Cao, L.; Su, L.; Wang, Y.; Chou, L.-Y.; Xie, J. Solid-State Synthesis of Defect-Rich Zr-UiO-66 Metal−Organic Framework Nanoparticles for the Catalytic Ring Opening of Epoxides with Alcohols. *ACS Appl. Nano Mater.* **2021**, *4*, 9752−9759.

(25) Øien, S.; Wragg, D.; Reinsch, H.; Svelle, S.; Bordiga, S.; Lamberti, C.; Lillerud, K. P. Detailed Structure Analysis of Atomic Positions and Defects in Zirconium Metal−Organic Frameworks. *Cryst. Growth Des.* **2014**, *14*, 5370−5372.

(26) Jiao, Y.; Liu, Y.; Zhu, G.; Hungerford, J. T.; Bhattacharyya, S.; Lively, R. P.; Sholl, D. S.; Walton, K. S. Heat-Treatment of Defective UiO-66 from Modulated Synthesis: Adsorption and Stability Studies. *J. Phys. Chem. C* **2017**, *121*, 23471−23479.

(27) Van de Voorde, B.; Stassen, I.; Bueken, B.; Vermoortele, F.; De Vos, D.; Ameloot, R.; Tan, J.-C.; Bennett, T. D. Improving the mechanical stability of zirconium-based metal−organic frameworks by incorporation of acidic modulators. *J. Mater. Chem. A* **2015**, *3*, 1737−1742.

(28) Vermoortele, F.; Bueken, B.; Le Bars, G.; Van de Voorde, B.; Vandichel, M.; Houthoofd, K.; Vimont, A.; Daturi, M.; Waroquier, M.; Van Speybroeck, V.; Kirschhock, C.; De Vos, D. E. Synthesis Modulation as a Tool To Increase the Catalytic Activity of Metal−Organic Frameworks: The Unique Case of UiO-66(Zr). *J. Am. Chem. Soc.* **2013**, *135*, 11465−11468.

(29) Tang, J.; Li, S.; Su, Y.; Chu, Y.; Xu, J.; Deng, F. Quantitative Analysis of Linker Composition and Spatial Arrangement of Multivariate Metal−Organic Framework UiO-66 through ^{1}H Fast MAS NMR. *J. Phys. Chem. C* **2020**, *124*, 17640−17647.

(30) Devautour-Vinot, S.; Maurin, G.; Serre, C.; Horcajada, P.; Paula da Cunha, D.; Guillerm, V.; de Souza Costa, E.; Taulelle, F.; Martineau, C. Structure and Dynamics of the Functionalized MOF Type UiO-66(Zr): NMR and Dielectric Relaxation Spectroscopies Coupled with DFT Calculations. *Chem. Mater.* **2012**, *24*, 2168−2177.

(31) Nandy, A.; Forse, A. C.; Witherspoon, V. J.; Reimer, J. A. NMR Spectroscopy Reveals Adsorbate Binding Sites in the Metal−Organic Framework UiO-66(Zr). *J. Phys. Chem. C* **2018**, *122*, 8295−8305.

(32) Xiao, Y.; Chu, Y.; Li, S.; Su, Y.; Tang, J.; Xu, J.; Deng, F. Primary Adsorption Sites of Light Alkanes in Multivariate UiO-66 at Room Temperature as Revealed by Solid-State NMR. *J. Phys. Chem. C* **2020**, *124*, 3738−3746.

(33) Venel, F.; Volkringer, C.; Lafon, O.; Pourpoint, F. Probing adsorption of water and DMF in UiO-66(Zr) using solid-state NMR. *Solid State Nucl. Magn. Reson.* **2022**, *120*, 101797.

(34) Venel, F.; Giovine, R.; Laurencin, D.; Špačková, J.; Mittelette, S.; Métro, T.; Volkringer, C.; Lafon, O.; Pourpoint, F. Probing oxygen exchange between UiO-66(Zr) MOF and water using ^{17}O solid-state NMR. *Chem.—Eur. J.* **2024**, *30*, No. e202302731.

(35) He, P.; Xu, J.; Terskikh, V. V.; Sutrisno, A.; Nie, H.-Y.; Huang, Y. Identification of Nonequivalent Framework Oxygen Species in

https://doi.org/10.1021/jacs.5c13805
J. Am. Chem. Soc. 2025, 147, 44200−44215

Metal−Organic Frameworks by ^{17}O Solid-State NMR. *J. Phys. Chem. C* **2013**, *117*, 16953−16960.
(36) Khudozhitkov, A. E.; Jobic, H.; Kolokolov, D. I.; Freude, D.; Haase, J.; Stepanov, A. G. Probing the Guest-Mediated Structural Mobility in the UiO-66(Zr) Framework by ^{2}H NMR Spectroscopy. *J. Phys. Chem. C* **2017**, *121*, 11593−11600.
(37) Nadol, A.; Venel, F.; Giovine, R.; Leloire, M.; Volkringer, C.; Loiseau, T.; Gervais, C.; Mellot-Draznieks, C.; Doumert, B.; Trebosc, J.; Lafon, O.; Pourpoint, F. Probing the water adsorption and stability under steam flow of Zr-based metal-organic frameworks using ^{91}Zr solid-state NMR spectroscopy. *Chem. Sci.* **2024**, *16*, 69−82.
(38) Zhang, W.; Lucier, B. E. G.; Martins, V.; Azizivahed, T.; Hung, I.; Xu, Y.; Gan, Z.; Venkatesh, A.; Goh, T. W.; Huang, W.; Rossini, A. J.; Huang, Y. Local order, disorder, and everything in between: using ^{91}Zr solid-state NMR spectroscopy to probe zirconium-based metal-organic frameworks. *Phys. Chem. Chem. Phys.* **2025**, *27*, 4704−4716.
(39) Lucier, B. E. G.; Huang, Y., Chapter Five - A Review of ^{91}Zr Solid-State Nuclear Magnetic Resonance Spectroscopy. In *Annual Reports on NMR Spectroscopy*; Webb, G. A., Ed.; Academic Press, 2015; Vol. *84*, pp 233−289.
(40) Cliffe, M. J.; Wan, W.; Zou, X.; Chater, P. A.; Kleppe, A. K.; Tucker, M. G.; Wilhelm, H.; Funnell, N. P.; Coudert, F.-X.; Goodwin, A. L. Correlated defect nanoregions in a metal−organic framework. *Nat. Commun.* **2014**, *5*, 4176.
(41) Atzori, C.; Shearer, G. C.; Maschio, L.; Civalleri, B.; Bonino, F.; Lamberti, C.; Svelle, S.; Lillerud, K. P.; Bordiga, S. Effect of Benzoic Acid as a Modulator in the Structure of UiO-66: An Experimental and Computational Study. *J. Phys. Chem. C* **2017**, *121*, 9312−9324.
(42) Bueken, B.; Van Velthoven, N.; Krajnc, A.; Smolders, S.; Taulelle, F.; Mellot-Draznieks, C.; Mali, G.; Bennett, T. D.; De Vos, D. Tackling the Defect Conundrum in UiO-66: A Mixed-Linker Approach to Engineering Missing Linker Defects. *Chem. Mater.* **2017**, *29*, 10478−10486.
(43) Cliffe, M. J.; Castillo-Martínez, E.; Wu, Y.; Lee, J.; Forse, A. C.; Firth, F. C. N.; Moghadam, P. Z.; Fairen-Jimenez, D.; Gaultois, M. W.; Hill, J. A.; Magdysyuk, O. V.; Slater, B.; Goodwin, A. L.; Grey, C. P. Metal−Organic Nanosheets Formed via Defect-Mediated Transformation of a Hafnium Metal−Organic Framework. *J. Am. Chem. Soc.* **2017**, *139*, 5397−5404.
(44) Bennett, T. D.; Todorova, T. K.; Baxter, E. F.; Reid, D. G.; Gervais, C.; Bueken, B.; Van de Voorde, B.; De Vos, D.; Keen, D. A.; Mellot-Draznieks, C. Connecting defects and amorphization in UiO-66 and MIL-140 metal-organic frameworks: a combined experimental and computational study. *Phys. Chem. Chem. Phys.* **2016**, *18*, 2192−2201.
(45) Gómez-Avilés, A.; Solís, R. R.; García-Frutos, E. M.; Bedia, J.; Belver, C. Novel isoreticular UiO-66-NH2 frameworks by N-cycloalkyl functionalization of the 2-aminoterephtalate linker with enhanced solar photocatalytic degradation of acetaminophen. *Chem. Eng. J.* **2023**, *461*, 141889.
(46) Cao, H.; Dou, M.; Lyu, Z.; Wang, Y.; Pedersen, C. M.; Qiao, Y. Understanding the interaction mechanism of carbazole/anthracene with N,N-dimethylformamide: NMR study substantiated carbazole separation. *Ind. Chem. Mater.* **2023**, *1*, 240−246.
(47) Wang, J.; Jiang, J.-Z.; Chen, W.; Bai, Z.-W. Data of $^{1}H/^{13}C$ NMR spectra and degree of substitution for chitosan alkyl urea. *Data Brief* **2016**, *7*, 1228−1236.
(48) Svobodová, H.; Nonappa; Lahtinen, M.; Wimmer, Z.; Kolehmainen, E. A steroid-based gelator of A(LS)2 type: tuning gel properties by metal coordination. *Soft Matter* **2012**, *8*, 7840−7847.
(49) Samanta, S.; Raval, P.; Manjunatha Reddy, G. N.; Chaudhuri, D. Cooperative Self-Assembly Driven by Multiple Noncovalent Interactions: Investigating Molecular Origin and Reassessing Characterization. *ACS Cent. Sci.* **2021**, *7*, 1391−1399.
(50) Volkringer, C.; Loiseau, T.; Guillou, N.; Ferey, G.; Haouas, M.; Taulelle, F.; Elkaim, E.; Stock, N. High-throughput aided synthesis of the porous metal-organic framework-type aluminum pyromellitate, MIL-121, with extra carboxylic acid functionalization. *Inorg. Chem.* **2010**, *49*, 9852−9862.
(51) Haouas, M.; Volkringer, C.; Loiseau, T.; Férey, G.; Taulelle, F. Monitoring the Activation Process of the Giant Pore MIL-100(Al) by Solid State NMR. *J. Phys. Chem. C* **2011**, *115*, 17934−17944.
(52) Brown, S. P. Applications of high-resolution ^{1}H solid-state NMR. *Solid State Nucl. Magn. Reson.* **2012**, *41*, 1−27.
(53) Shearer, G. C.; Forselv, S.; Chavan, S.; Bordiga, S.; Mathisen, K.; Bjørgen, M.; Svelle, S.; Lillerud, K. P. In Situ Infrared Spectroscopic and Gravimetric Characterisation of the Solvent Removal and Dehydroxylation of the Metal Organic Frameworks UiO-66 and UiO-67. *Top. Catal.* **2013**, *56*, 770−782.
(54) Vandichel, M.; Hajek, J.; Ghysels, A.; De Vos, A.; Waroquier, M.; Van Speybroeck, V. Water coordination and dehydration processes in defective UiO-66 type metal organic frameworks. *CrystEngComm* **2016**, *18*, 7056−7069.
(55) Rossini, A. J.; Mills, R. W.; Briscoe, G. A.; Norton, E. L.; Geier, S. J.; Hung, I.; Zheng, S.; Autschbach, J.; Schurko, R. W. Solid-State Chlorine NMR of Group IV Transition Metal Organometallic Complexes. *J. Am. Chem. Soc.* **2009**, *131*, 3317−3330.
(56) Zhang, W.; Lucier, B. E. G.; Willans, M. J.; Huang, Y. ^{35}Cl NMR of Metal-Organic Frameworks: What Can We Learn? *Chem. Methods* **2025**, *5*, No. e202400078.
(57) Widdifield, C. M.; Chapman, R. P.; Bryce, D. L. Chlorine, bromine, and iodine solid-state NMR spectroscopy. *Annu. Rep. NMR Spectrosc.* **2009**, *66*, 195−326.
(58) Rossini, A. J.; Hung, I.; Johnson, S. A.; Slebodnick, C.; Mensch, M.; Deck, P. A.; Schurko, R. W. Solid-State ^{91}Zr NMR Spectroscopy Studies of Zirconocene Olefin Polymerization Catalyst Precursors. *J. Am. Chem. Soc.* **2010**, *132*, 18301−18317.
(59) O'Dell, L. A.; Rossini, A. J.; Schurko, R. W. Acquisition of ultra-wideline NMR spectra from quadrupolar nuclei by frequency stepped WURST−QCPMG. *Chem. Phys. Lett.* **2009**, *468*, 330−335.
(60) Koschnick, C.; Stäglich, R.; Scholz, T.; Terban, M. W.; von Mankowski, A.; Savasci, G.; Binder, F.; Schökel, A.; Etter, M.; Nuss, J.; Siegel, R.; Germann, L. S.; Ochsenfeld, C.; Dinnebier, R. E.; Senker, J.; Lotsch, B. V. Understanding disorder and linker deficiency in porphyrinic zirconium-based metal−organic frameworks by resolving the Zr_8O_6 cluster conundrum in PCN-221. *Nat. Commun.* **2021**, *12*, 3099.
(61) He, P.; Lucier, B. E. G.; Terskikh, V. V.; Shi, Q.; Dong, J.; Chu, Y.; Zheng, A.; Sutrisno, A.; Huang, Y. Spies Within Metal-Organic Frameworks: Investigating Metal Centers Using Solid-State NMR. *J. Phys. Chem. C* **2014**, *118*, 23728−23744.
(62) Sharma, A.; Varshney, M.; Chae, K. H.; Shin, H. J.; Won, S. O. Investigation on the local electronic/atomic structure properties using XANES/EXAFS and photocatalyst application of $Zr_{1-x}Cu_xO_2$ ($0 \leq x \leq 0.2$). *Curr. Appl. Phys.* **2016**, *16*, 1326−1333.
(63) Choy, J.-H.; Yoon, J.-B.; Park, J.-H. In situ XAFS study at the Zr K-edge for SiO_2/ZrO_2 nano-sol. *J. Synchrotron Radiat.* **2001**, *8*, 782−784.
(64) Semivrazhskaya, O. O.; Salionov, D.; Clark, A. H.; Casati, N. P. M.; Nachtegaal, M.; Ranocchiari, M.; Bjelić, S.; Verel, R.; van Bokhoven, J. A.; Sushkevich, V. L. Deciphering the Mechanism of Crystallization of UiO-66 Metal-Organic Framework. *Small* **2023**, *19*, No. e2305771.
(65) Jakobsen, S.; Gianolio, D.; Wragg, D. S.; Nilsen, M. H.; Emerich, H.; Bordiga, S.; Lamberti, C.; Olsbye, U.; Tilset, M.; Lillerud, K. P. Structural determination of a highly stable metal-organic framework with possible application to interim radioactive waste scavenging: Hf-UiO-66. *Phys. Rev. B: Condens. Matter Mater. Phys.* **2012**, *86*, 125429.
(66) Perras, F. A.; Venkatesh, A.; Hanrahan, M. P.; Goh, T. W.; Huang, W.; Rossini, A. J.; Pruski, M. Indirect detection of infinite-speed MAS solid-state NMR spectra. *J. Magn. Reson.* **2017**, *276*, 95−102.
(67) Kobayashi, T.; Perras, F. A.; Goh, T. W.; Metz, T. L.; Huang, W.; Pruski, M. DNP-Enhanced Ultrawideline Solid-State NMR Spectroscopy: Studies of Platinum in Metal−Organic Frameworks. *J. Phys. Chem. Lett.* **2016**, *7*, 2322−2327.

(68) Venkatesh, A.; Lund, A.; Rochlitz, L.; Jabbour, R.; Gordon, C. P.; Menzildjian, G.; Viger-Gravel, J.; Berruyer, P.; Gajan, D.; Copéret, C.; Lesage, A.; Rossini, A. J. The Structure of Molecular and Surface Platinum Sites Determined by DNP-SENS and Fast MAS ^{195}Pt Solid-State NMR Spectroscopy. *J. Am. Chem. Soc.* **2020**, *142*, 18936−18945.
(69) Venkatesh, A.; Gioffrè, D.; Atterberry, B. A.; Rochlitz, L.; Carnahan, S. L.; Wang, Z.; Menzildjian, G.; Lesage, A.; Copéret, C.; Rossini, A. J. Molecular and Electronic Structure of Isolated Platinum Sites Enabled by the Expedient Measurement of ^{195}Pt Chemical Shift Anisotropy. *J. Am. Chem. Soc.* **2022**, *144*, 13511−13525.
(70) Koppe, J.; Yakimov, A. V.; Gioffrè, D.; Usteri, M.-E.; Vosegaard, T.; Pintacuda, G.; Lesage, A.; Pell, A. J.; Mitchell, S.; Pérez-Ramírez, J.; Copéret, C. Coordination environments of Pt single-atom catalysts from NMR signatures. *Nature* **2025**, *642*, 613−619.
(71) Zhao, X.; Zheng, M.; Zhang, Z.; Wang, Y.; Zhou, Y.; Zhou, X.; Zhang, H. Supramolecular Nanosheet evolution into BC3N matrix improves the hydrogen evolution reaction activity in the pH universality of highly dispersed Pt nanoparticles. *J. Mater. Chem. A* **2021**, *9*, 16427−16435.
(72) Luo, F.; Pan, S.; Xie, Y.; Li, C.; Yu, Y.; Bao, H.; Yang, Z. Hydrazine-Assisted Acidic Water Splitting Driven by Iridium Single Atoms. *Adv. Sci.* **2023**, *10*, 2305058.

https://doi.org/10.1021/jacs.5c13805
J. Am. Chem. Soc. 2025, 147, 44200−44215